



# Intrinsic efficiency limits in low-bandgap non-fullerene acceptor organic solar cells

Safakath Karuthedath<sup>1,5</sup>, Julien Gorenflot<sup>1,5</sup>, Yuliar Firdaus<sup>1</sup>, Neha Chaturvedi<sup>1</sup>, Catherine S. P. De Castro<sup>1,5</sup>, George T. Harrison<sup>1</sup>, Jafar I. Khan<sup>1</sup>, Anastasia Markina<sup>2</sup>, Ahmed H. Balawi<sup>1</sup>, Top Archie Dela Peña<sup>1</sup>, Wenlan Liu<sup>2</sup>, Ru-Ze Liang<sup>1</sup>, Anirudh Sharma<sup>1</sup>, Sri H. K. Paleti<sup>1</sup>, Weimin Zhang<sup>1</sup>, Yuanbao Lin<sup>1</sup>, Erkki Alarousu<sup>1</sup>, Dalaver H. Anjum<sup>3</sup>, Pierre M. Beaujuge<sup>1</sup>, Stefaan De Wolf<sup>1</sup>, Iain McCulloch<sup>1,4</sup>, Thomas D. Anthopoulos<sup>1</sup>, Derya Baran<sup>1</sup>, Denis Andrienko<sup>2</sup>✉ and Frédéric Laquai<sup>1</sup>✉

**In bulk heterojunction (BHJ) organic solar cells (OSCs) both the electron affinity (EA) and ionization energy (IE) offsets at the donor-acceptor interface should equally control exciton dissociation. Here, we demonstrate that in low-bandgap non-fullerene acceptor (NFA) BHJs ultrafast donor-to-acceptor energy transfer precedes hole transfer from the acceptor to the donor and thus renders the EA offset virtually unimportant. Moreover, sizeable bulk IE offsets of about 0.5 eV are needed for efficient charge transfer and high internal quantum efficiencies, since energy level bending at the donor-NFA interface caused by the acceptors' quadrupole moments prevents efficient exciton-to-charge-transfer state conversion at low IE offsets. The same bending, however, is the origin of the barrier-less charge transfer state to free charge conversion. Our results provide a comprehensive picture of the photophysics of NFA-based blends, and show that sizeable bulk IE offsets are essential to design efficient BHJ OSCs based on low-bandgap NFAs.**

The minimum driving force required for efficient charge separation in bulk heterojunction (BHJ) organic solar cells (OSCs) has remained controversial<sup>1–9</sup>. In BHJs with low-bandgap non-fullerene acceptors (NFAs) both the electron donor and acceptor harvest photons, preferably in complementary spectral regions. Consequently, two channels of charge generation are expected, electron transfer from the donor to the acceptor and hole transfer from the acceptor to the donor. In thin-film BHJs, the former is driven by the electron affinity (EA) offset, the latter by the ionization energy (IE) offset.

In fullerene-based systems, the requirement of a minimal EA offset of around 0.3 eV was experimentally identified<sup>10</sup> and repeatedly confirmed<sup>11–14</sup>. However, recent reports of efficient NFA-based BHJs indicate that this requirement may not hold for NFAs. Indeed, a number of studies concluded that charge generation in NFA BHJs can be efficient even for zero offsets, contrary to fullerene-based systems<sup>10–13</sup>. Moreover, negligible driving forces for charge separation via hole transfer<sup>8,9,15–18</sup> and electron transfer<sup>19–21</sup> are often used as an explanation of low-energy losses in high-performing NFA blends<sup>22</sup>.

To determine IE and EA, characterization techniques such as ultraviolet photoelectron spectroscopy (UPS), photoemission spectroscopy in air and cyclic voltammetry have been used. Notably, only cyclic voltammetry supports the idea of zero IE<sup>8,9,15–18</sup> and EA<sup>19–21</sup> offsets. However, cyclic voltammetry does not provide reliable estimates of IEs and EAs of solid films<sup>23</sup>. PM6:Y6, for example, has zero offset according to cyclic voltammetry, but 0.5 eV when measured by UPS<sup>9</sup>. Apart from putting the necessity for a type-II

heterojunction into question, efficient charge generation with zero energy offsets implies that the mechanisms of charge generation in NFA- and fullerene-based blends are different<sup>24</sup>. A few recent studies acknowledged that IE offsets are important for charge generation<sup>1,25,26</sup>, demonstrating an increase of the charge generation efficiency with the IE offset, yet only for a very limited number of structurally related systems.

A coherent study providing uniform characterization of a large NFA series as well as a model explaining the origin of the IE-offset dependence in NFA-based systems and the recently reported barrier-less charge separation in NFA blends<sup>27</sup> is still missing, but needed for further optimization of energetic losses and internal quantum efficiency (IQE) of NFA BHJs<sup>28</sup>.

Here, we demonstrate that the exciton-to-charge conversion efficiency (and, therefore, the IQE) of low-bandgap NFA-based BHJ solar cells increases with the donor–NFA IE offset, reaching its maximum for offsets of ~0.5 eV. Charge generation does not depend on the EA offset. This is explained by ultrafast energy transfer from the donor to the acceptor. Indeed, by design, the photoluminescence (PL) of the higher bandgap donor overlaps with the absorption of the lower bandgap acceptor. This design principle broadens the BHJ's photoactive spectral region and thereby increases the maximum available short-circuit current density, and it facilitates Förster resonance energy transfer (FRET) from the donor to the NFA<sup>29–32</sup>. Consequently, FRET is the main deactivation channel for donor excitons in NFA BHJs. In fullerene BHJs, FRET is limited by the low oscillator strength of fullerene molecules<sup>33</sup>.

<sup>1</sup>KAUST Solar Center, Physical Sciences and Engineering Division (PSE), Materials Science and Engineering Program (MSE), King Abdullah University of Science and Technology (KAUST), Thuwal, Kingdom of Saudi Arabia. <sup>2</sup>Max Planck Institute for Polymer Research, Mainz, Germany. <sup>3</sup>Imaging and Characterization Core Laboratory, King Abdullah University of Science and Technology (KAUST), Thuwal, Kingdom of Saudi Arabia. <sup>4</sup>Department of Chemistry, University of Oxford, Oxford, UK. <sup>5</sup>These authors contributed equally: Safakath Karuthedath, Julien Gorenflot, Catherine S. P. De Castro.

✉e-mail: [denis.andrienko@mpip-mainz.mpg.de](mailto:denis.andrienko@mpip-mainz.mpg.de); [frederic.laquai@kaust.edu.sa](mailto:frederic.laquai@kaust.edu.sa)

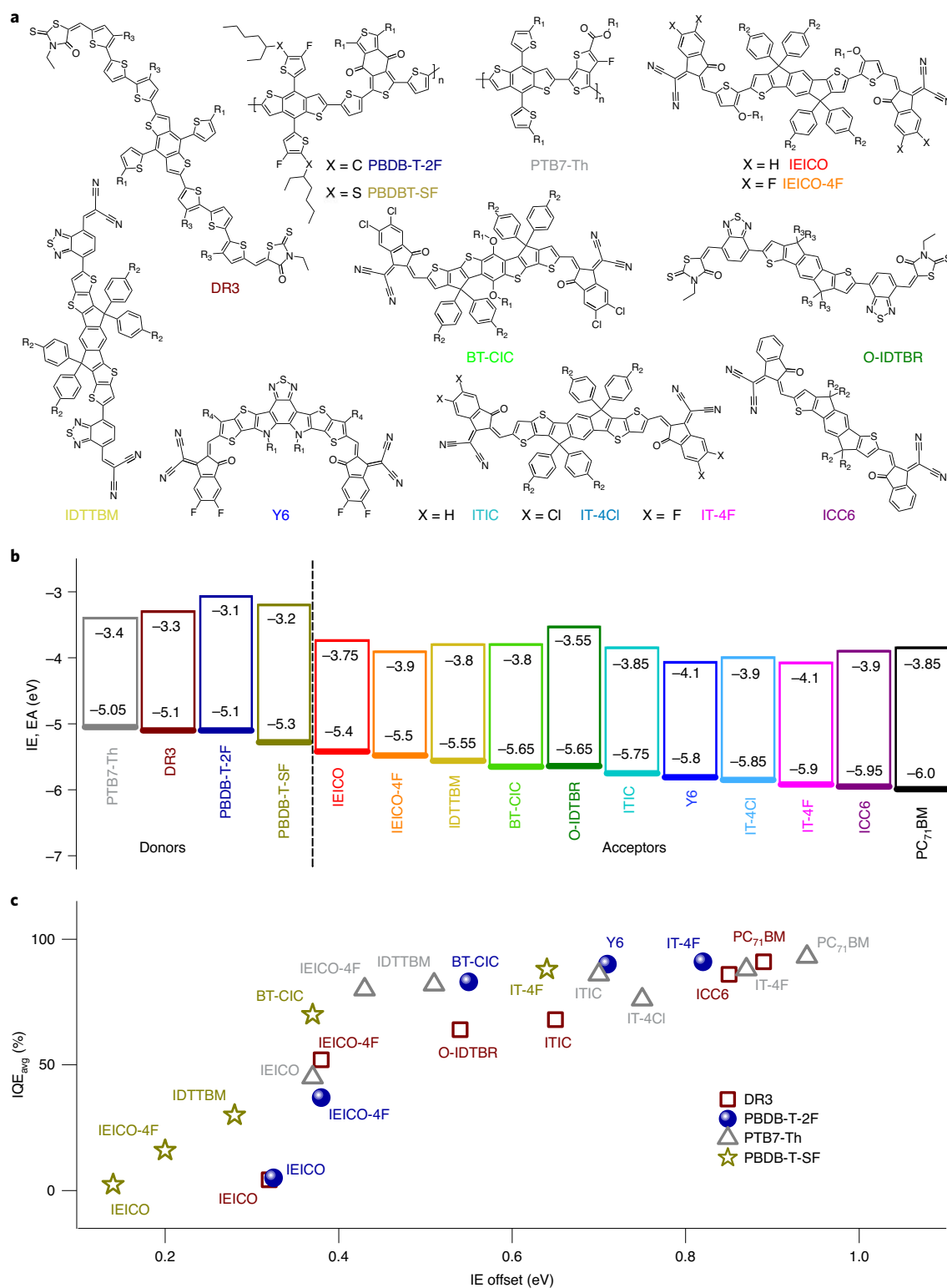


**Fig. 1 | Materials' structures, energy levels and IQEs in photovoltaic devices. a**, Chemical structures of the donor materials and NFAs investigated in this study.  $R_1$ ,  $-\text{CH}(\text{C}_4\text{H}_9)(\text{C}_2\text{H}_5)$ ;  $R_2$ ,  $-\text{C}_6\text{H}_{13}$ ;  $R_3$ ,  $-\text{C}_8\text{H}_{17}$  and  $R_4$ ,  $-\text{C}_{11}\text{H}_{23}$ . **b**, IE (thick horizontal lines) determined by UPS and EA (thin horizontal lines) by IPES. **c**, Spectrally averaged IQE ( $\text{IQE}_{\text{avg}}$ ) of optimized BHJ donor-NFA devices as a function of the IE offset between donor and acceptor for the small molecule donor DR3 and the donor polymers PBDB-T-2F, PTB7-Th and PBDB-T-SF. For OSC device data and preparation conditions, we refer to the Extended Data Figs. 4–6 and Supplementary Tables 2–4.

Furthermore, we demonstrate that bending of the energy levels at the donor–acceptor heterojunction, caused by the acceptors' quadrupole moments, increases the interfacial charge-transfer (CT)

state energy. If this energy level bending is not counterbalanced by the IE offset, then it creates a barrier for exciton-to-CT state conversion. The same energy level bending, however, leads to

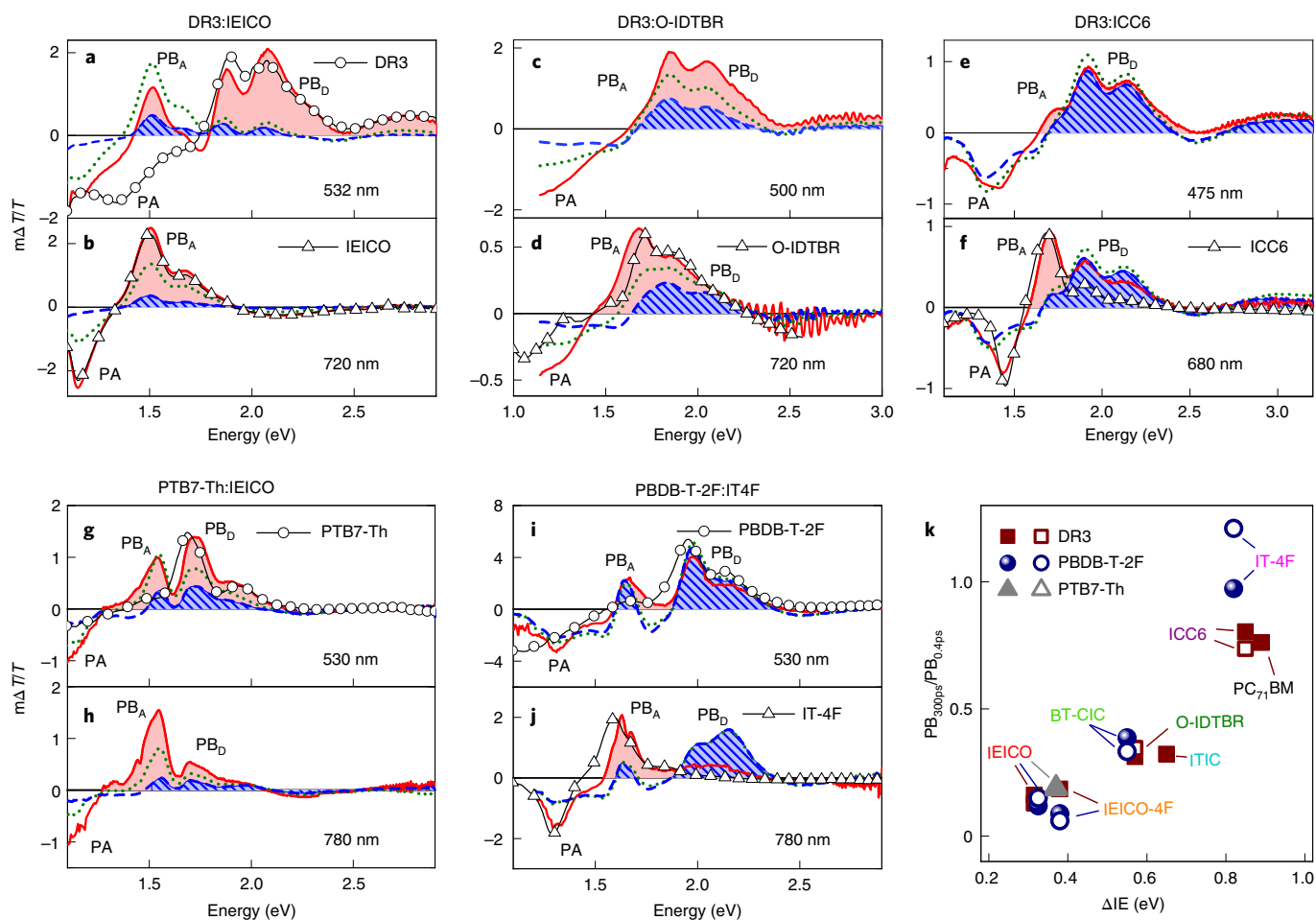


**Fig. 2 | The charge carrier generation yield is independent of donor or acceptor excitation, but it increases with the IE offset. a–j,** Picosecond–nanosecond TA spectra of selected neat donors (circles), neat acceptors (triangles) and blends after 0.4 ps (red solid line), 30 ps (green dotted line) and 300 ps (blue dashed line): DR3:IEICO (a,b), DR3:O-IDTBR (c,d), DR3:ICC6 (e,f), PTB7-Th:IEICO (g,h) and PBDB-T-2F:IT-4F (i,j) blend films after selective excitation of donor (a,c,e,g,i) and acceptor molecules (b,d,f,h,j) at the wavelength indicated in the figure. **k,** Ratio of the integrated photobleach (after 300 ps) to the initial photobleach (0.4–0.7 ps) ( $PB_{300ps}/PB_{0.4ps}$ ) of all investigated blends for absorbed fluences of  $\sim 1.6\text{--}4\ \mu\text{J cm}^{-2}$ , with donor (open symbols) and acceptor (closed symbols) excitation, as a function of the IE offset ( $\Delta IE$ ). The integrated areas are shaded in the example spectra (a–j): unpatterned red for the initial bleach, and striped blue for the bleach at 300 ps. The spectra for the blends not represented here can be found in Supplementary Figs. 4 and 7.

barrier-less CT state to free charge conversion, as recently observed experimentally<sup>27,34</sup>. The energy level bending also explains the presence of energetically high-lying CT states reported for many NFA-based systems.

A straightforward implication of our study is a clear design principle for NFA materials: high exciton-to-charge conversion yields can only be achieved for sizeable ( $\sim 0.5\text{ eV}$ ) bulk IE offsets, since only they provide sufficient driving force for dissociation of excitons to CT states, and further to separated charge carriers.

To reveal the impact of IE, EA and FRET on charge generation in NFA BHJs, we studied representative donor–acceptor combinations: the small molecule electron donor DR3TBDTT (DR3)<sup>35</sup>, the widely used donor polymers PTB7-Th (PCE10) and PBDB-T-SF (PCE13)<sup>36</sup>, and the recently reported high-efficiency donor polymer PBDB-T-2F (PM6)<sup>37</sup>. Ten small molecule NFAs were selected as acceptors, including Y6, one of the current state-of-the-art NFAs, as well as PC<sub>71</sub>BM as reference<sup>38</sup>. Chemical structures of all materials are shown in Fig. 1 alongside their IE and EA values, determined by UPS and inverse photoemission spectroscopy (IPES), respectively, as well as the average IQEs of respective BHJs (see UPS and low-energy-IPES (LE-IPES) spectra in Extended Data Figs. 1–3, and Supplementary Table 1)<sup>39</sup>. Since IE offsets are essential in our

study, we confirmed the materials' IEs by another technique, photoemission spectroscopy in air (Supplementary Fig. 1)<sup>39,40</sup>.

First, one intriguing observation is that the IQE averaged over the range of absorption of the BHJ, increases with the IE offset, as shown in Fig. 1c. Second, IQEs are practically independent of donor or acceptor excitation (see IQE spectra in Extended Data Fig. 5). This indicates that the same process governs the quantum efficiency, even though charge generation is expected to occur via electron transfer when exciting the donor, and hole transfer on acceptor excitation, the former determined by the EA offset, the latter by the IE offset. In other words, the IE offset determines the IQE even when selectively exciting the donor, and despite large EA offsets in all systems. Third, the device fill factor, a measure of the field dependence of charge generation, increases with the IE offset as well, suggesting that in low offset systems, charge generation exhibits a stronger dependence on the external bias (Extended Data Fig. 6).

To reveal the underlying reasons, we monitored the dynamics of excited states by transient absorption (TA) spectroscopy. Figure 2 shows TA spectra of selected thin-film blends after selective donor or acceptor photoexcitation. Further TA data can be found in Supplementary Figs. 4 and 7. Clearly, donor and acceptor photoexcitation initially generate different excited states: donor

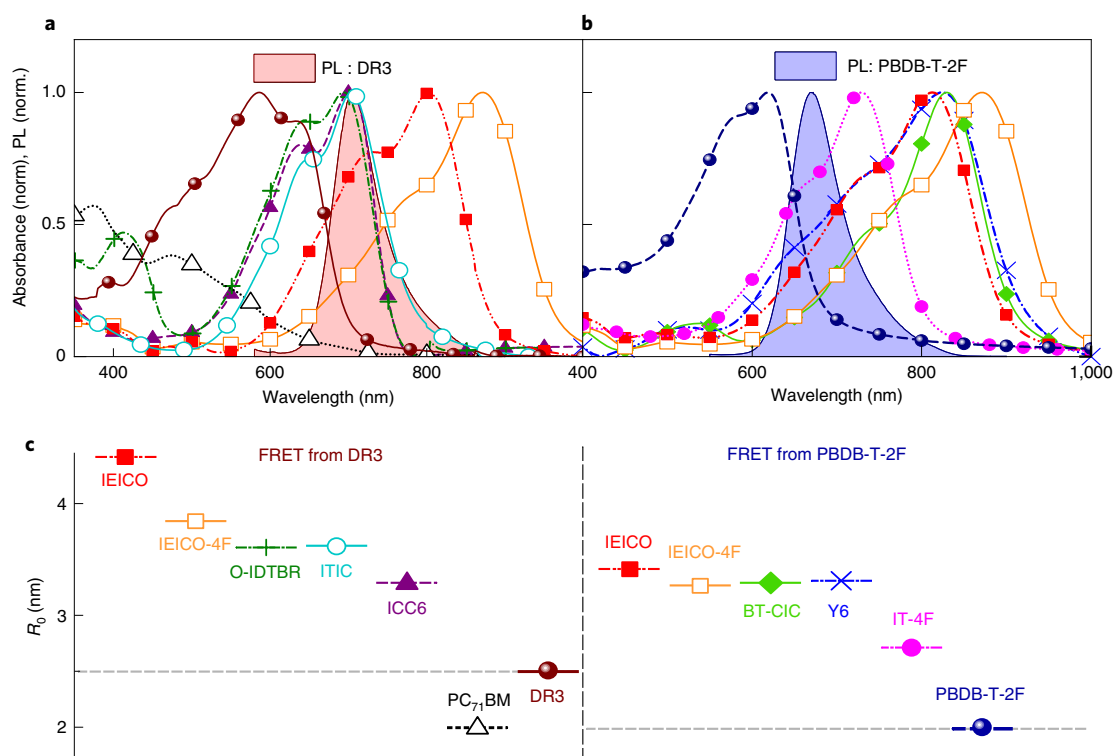


**Fig. 3 | Spectral overlap of donor PL and acceptor absorption facilitates ultrafast energy transfer.** **a, b**, Normalized UV-vis absorption spectra of acceptors (continuous lines) (**a**) used with DR3 as donor (dashed line) and acceptors (**b**) used with PBDB-T-2F as donor and PL spectra of DR3 and PBDB-T-2F (filled curves) as indicated by the legends. **c**, FRET radii for DR3- and PBDB-T-2F-based blends as well as within the donor phase.

excitation leads to photobleaching of the donor's ground state absorption ( $PB_D$  in Fig. 2), as well as to photoinduced absorption. Excitation of the acceptor, on the other hand, initially bleaches the ground state absorption of the acceptor only ( $PB_A$  in Fig. 2), associated with photoinduced absorption features resembling the excitonic signatures of neat acceptor films. While donor and acceptor photoexcitation initially generate different excited states (see red lines for the initial TA spectra in Fig. 2), virtually similar TA spectra are observed after 300 ps (blue lines in Fig. 2). We attribute this to charge generation, however, not in the case of DR3:IEICO and PBDB-T-2F:IEICO, which we discuss below.

To compare the excited state evolution after donor and acceptor excitation, we integrated the ground state bleach over the entire photobleached region (shaded areas in Fig. 2). Quantitatively, the relative photobleached area (indicating the overall excitation density) after charge generation is completed (probed at 300 ps) compared to the initial photobleach area (probed at 0.4 ps), does not depend on donor or acceptor excitation, but it increases with the IE offset (Fig. 2k).

DR3:IEICO and PBDB-T-2F:IEICO blends are, however, very different. As shown in Fig. 2a, within 30 ps after donor photoexcitation (green line), the initially convoluted exciton-induced absorption signatures of donor and acceptor have evolved into exciton-induced absorption of the acceptor, while only marginal charge generation is observed. Besides, acceptor excitons created by direct photoexcitation of the acceptor subsequently decay to the ground state without undergoing charge transfer. We conclude that almost exclusively energy transfer (FRET) from the donor to the acceptor IEICO takes place, while hole transfer to the donor is inefficient. This is supported by steady-state PL quenching measurements, which show poor PL quenching on acceptor excitation, and acceptor PL on donor photoexcitation (Supplementary Fig. 15), supporting FRET occurs in these systems. We note that PL quenching

efficiencies in the other blends are larger. This low exciton quenching efficiency in DR3:IEICO and PBDB-T-2F:IEICO blends cannot be attributed to morphological differences between the blends. In fact, we have evidence that all donor-acceptor blends are intimately mixed from transmission electron microscopy (TEM) combined with electron energy-loss spectroscopy (EELS) and scanning TEM (Supplementary Fig. 18 and Extended Data Fig. 9), showing no indication of component demixing that could satisfactorily explain the inefficient exciton quenching. Second, in more inter-mixed as-cast DR3:IEICO blends, obtained without solvent vapour annealing, even lower PL quenching efficiencies were observed on acceptor excitation and enhanced energy transfer on donor excitation (Supplementary Figs. 5 and 16).

The large overlap of donor PL and acceptor absorption, shown in Fig. 3a,b triggers efficient energy transfer in all donor-NFA systems. The FRET radii<sup>41,42</sup> (Supplementary Information Section VI) are larger for the donor-NFA pairs than for the respective donor-donor pairs (Fig. 3c). This indicates that when approaching the donor-acceptor interface, an exciton in the donor is more likely to transfer to an acceptor than to reach the interface to undergo electron transfer. More precisely, for donor excitons at a distance of 1 nm from the interface, the calculated FRET rates are of the order of  $10^{13} \text{ s}^{-1}$  in all donor-NFA systems (Supplementary Information Section VI). This indicates that FRET competes with donor-acceptor electron transfer at shorter distances, as suggested very recently<sup>29</sup>.

Indeed, FRET from DR3 to NFA could clearly be observed in solution (Supplementary Fig. 8). In films, however, it is instantaneously followed by hole transfer from the acceptor to the donor. We confirmed ultrafast hole transfer in diluted DR3:NFA (95:5) blends on selective excitation of the acceptor, which resulted in a rise of the donor signal within the response time of our TA setup of a few hundred femtoseconds (Supplementary Fig. 9) in line with a recent study<sup>34</sup>.

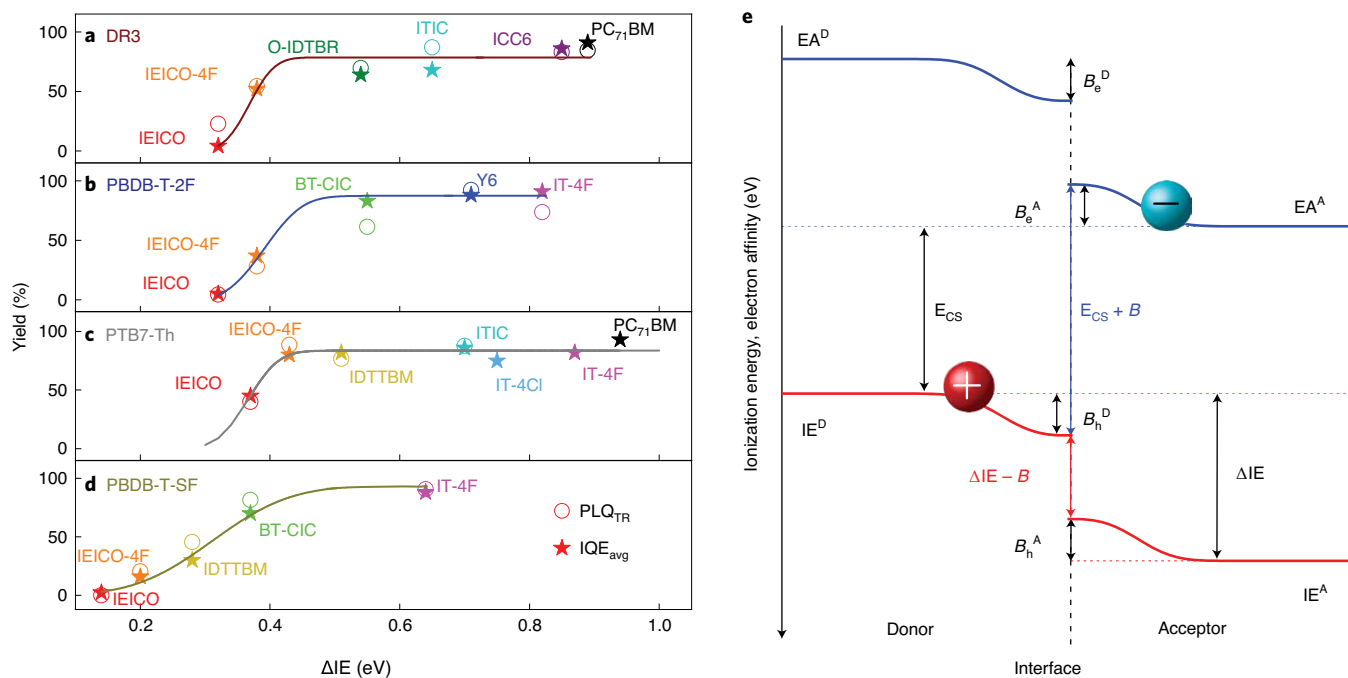


**Fig. 4 | The IQE follows the exciton quenching yield controlled by the IE offset and energy level bending at the donor-acceptor interface. a–d,** Average IQE ( $IQE_{avg}$ , stars) and exciton lifetime quenching  $1 - \tau_{blend}/\tau_{pristine}$  ( $PLQ_{TR}$ , circles) where  $\tau_{blend}$  and  $\tau_{pristine}$  are the PL lifetime of a blend and a pristine material film, respectively, as a function of IE offset ( $\Delta IE$ ) for DR3- (a), PBDB-T-2F- (b), PTB7-Th- (c) and PBDB-T-SF- (d) based blends (IQE spectra in Extended Data Fig. 5, PL spectra and transients in Extended Data Fig. 8 and Supplementary Figs. 12–14). The dependence corresponds to the fraction of the interface, which exhibits an energy bending lower than  $\Delta IE$ , assuming a Gaussian distribution of energy level bending with an average  $B$  and a standard deviation  $\sigma$ , we obtain  $IQE = \frac{IQE_{max}}{2} (1 + \operatorname{erfc} \frac{B - \Delta IE}{\sigma})$ . The fits to this function (solid lines in a–d) yield  $B = 0.37$  eV and  $\sigma = 0.04$  eV for DR3, 0.37 and 0.05 eV for PTB7-Th, 0.39 and 0.06 eV for PBDB-T-2F and 0.31 and 0.13 eV for PBDB-T-SF. **e,** Schematic of the energy level bending at the donor-acceptor heterojunction due to the electrostatic interaction of charges with quadrupole moments of surrounding molecules.

As a result of FRET, CT in blends is largely hole transfer from the acceptor to the donor, independent of donor or acceptor photoexcitation. This explains why donor and acceptor photoexcitation yield similar IQEs. Furthermore, it implies that the IQE depends on the driving force of the hole transfer reaction, governed by the difference between the singlet excited state energy of the acceptor and the blend's CT state.

The conversion efficiency of the acceptor exciton-to-free charges therefore controls the IQE. We identify the efficiency limit from the amount of acceptor exciton quenching efficiency determined by time-resolved PL (TRPL) experiments (Fig. 4a–d). The efficiency of exciton quenching closely follows the IQE, indicating that apart from the acceptor singlet exciton-to-CT state conversion, CT to free charge separation and carrier extraction are efficient. We emphasize that in NFA-based blends TRPL experiments can provide an immediate measure of the free charge generation efficiency and thus device IQE, unlike in fullerene-based systems, in which ultrafast and efficient exciton quenching does not necessarily indicate high free carrier yields and IQE due to the occurrence of other loss channels such as geminate charge pairs recombination. Finally, we stress that the correlation of PL quenching from TRPL and IQE cannot be explained by donor-acceptor demixing, as morphology does not follow energetic offsets and a coincidental correlation across such a large set of different donor-acceptor blends appears highly unlikely (see scanning TEM and EELS maps in Supplementary Fig. 18 and Extended Data Fig. 9).

Since the transition from the acceptor singlet exciton to the interfacial CT state is a hole transfer from the acceptor to the donor, it comes as little surprise that it depends on the IE offset. It is, however, surprising and unclear why a system-independent offset as

large as 0.3–0.4 eV is required to obtain a 50% CT yield and why the efficiency increase is less steep than that of a typical thermally activated process.

To explain both observations, we depict an energy level diagram of a solar cell in Fig. 4e. Here, the key difference to common diagrams is the bending of the IE and EA at the interface. This energy level bending is due to the gradual change in the electrostatic potential created by the quadrupole moments of the NFA and the donor polymer<sup>43–49</sup>. The energy level is bent in the direction that corresponds to the (negative) sign of the in-plane quadrupole moment of the acceptor-donor-acceptor NFA molecule. Because of energy level bending, the CT state energy increases, and the IE difference narrows by approximately the same amount at the interface. The energy level bending has no impact on the diffusion of excitons towards the interface, as both EA and IE in a material are bent in the same direction, leaving the energy gap within the acceptor (or donor) unchanged.

Energy level bending has a clear impact on the energetics of two-particle interactions of states involved in charge generation and separation: the excited state of the acceptor ( $A^*$ ), the CT state and the charge-separated state (CS). For the acceptor exciton,  $E^{A^*} = EA^A - IE^A - E_{Coulomb}^{A^*}$ , where  $E_{Coulomb}^{A^*}$  is the Coulomb interaction energy of the electron and hole, in the solid state. Different signs of energy level bending on the donor and acceptor sides increase the energy of the CT state to  $E^{CT} = EA_{interface}^A - IE_{interface}^D - E_{Coulomb}^{CT} = EA^A - IE^D + B - E_{Coulomb}^{CT}$ . Here  $E_{Coulomb}^{CT}$  is the Coulomb binding of a CT state at a perfectly flat interface (that is, without bending), and  $B = B_e^A + B_h^D$  is the bias potential, where the subscripts e and h represent electrons and holes, respectively, as depicted in Fig. 4e. Finally, the charge-separated state is not affected by the energy level

bending, since both electron and hole are apart from the interface,  $E^{\text{CS}} = EA^{\text{A}} - IE^{\text{D}}$ .

Next, we discuss the dissociation energy of the CT state, that is, the CT to charge-separated transition,  $\Delta E_{\text{CT} \rightarrow \text{CS}} = E^{\text{CS}} - E^{\text{CT}} = E_{\text{Coulomb}}^{\text{CT}} - B$ . Clearly, the interfacial bias reduces the dissociation energy of the CT state. In fact, the optimal condition is achieved for  $B = E_{\text{Coulomb}}^{\text{CT}} \approx 0.4$  eV, which then provides barrier-less dissociation, as demonstrated very recently for Y6 (ref. 27). Most of the reported blends provide sufficient bias to split the CT state, which explains their high efficiency.

We now turn to the excited to CT state transition. The driving force for this reaction,  $\Delta E_{\text{A}^* \rightarrow \text{CT}} = E^{\text{A}^*} - E^{\text{CT}} = \Delta IE - B - (E_{\text{Coulomb}}^{\text{A}^*} - E_{\text{Coulomb}}^{\text{CT}})$ , has three contributions. First, the offset between the IEs of the donor and the acceptor,  $\Delta IE = IE^{\text{D}} - IE^{\text{A}}$ . Second, the negative contribution of the bias potential, since the CT state energy is increased by the energy level bending (Fig. 4e). Third, the difference between the hole–electron binding energies of a Frenkel-type exciton and a CT state. It might seem that the last term provides a large negative contribution to the driving force, since it takes a substantial amount of energy to pull an electron and hole apart from each other during an excited to CT state transition, in a molecular dimer. However, polarizable force field calculations demonstrate that, in a solid-state, strong dielectric stabilization of two charges in a CT state compensates Coulomb binding of a Frenkel exciton, that is,  $E_{\text{Coulomb}}^{\text{A}^*} - E_{\text{Coulomb}}^{\text{CT}} \approx 0$ .

The consequence is that  $\Delta E_{\text{A}^* \rightarrow \text{CT}}$  is reduced to  $\Delta IE - B$ , which can be either positive or negative, depending on  $\Delta IE$ . This is experimentally confirmed by electroluminescence spectroscopy of NFA-based solar cells: BHJs with large  $\Delta IE$ , namely DR3:PCBM, DR3:ICC6, DR3:ITIC, PBDB-T-2F:IT-4F, exhibit a clear CT state electroluminescence emission observed at lower energy than the neat acceptor's electroluminescence, while no such CT state emission is observed in BHJs with low offsets (Extended Data Fig. 10 and Supplementary Fig. 21). We hypothesize that excitons reaching an interface that exhibits a negative  $\Delta E_{\text{A}^* \rightarrow \text{CT}}$  have the chance to diffuse back to the bulk of the acceptor phase. Hence, the exciton lifetime as measured by TRPL gradually becomes similar to that of a neat acceptor film when  $\Delta IE$  decreases (Fig. 4a–c).

To further understand the gradual increase of the IQE with the IE offset ( $\Delta IE$ ), we note that rough interfaces provide a broad spread of available interfacial biases. Assuming a Gaussian distribution of  $B$  and integrating the fraction of excited to CT state transitions for which  $\Delta IE - B$  is positive, we obtain  $\text{IQE} = \frac{\text{IQE}_{\text{max}}}{2} (1 + \text{erfc} \frac{B - \Delta IE}{\sigma})$ , where  $B$  is now the mean value of the bias potential and  $\text{erfc}$  represent the error function. The fit to this simple expression describes the experimentally observed IQE versus  $\Delta IE$  dependence very well across all investigated systems, as shown in Fig. 4a–d. The fits provide similar average energy level bending  $B$  for DR3, PTB7-Th and PBDB-T-2F as donors, precisely a  $B$  of  $\sim 380 \pm 10$  meV, standard deviation of the bending distribution  $\sigma$  of  $\sim 50 \pm 10$  meV and  $\text{IQE}_{\text{max}}$  of  $\sim 0.8 \pm 4\%$ . We note that for the PBDB-T-SF:NFA systems a smaller value of  $B$  of  $\sim 310$  meV with a broader distribution ( $\sigma = 130$  meV) is observed. However, this broader distribution leads to the same minimum IE offset of 0.5 eV required to efficiently split all the excitons as for the other donors as  $B + 2\sigma \sim 0.5$  eV. Within our model, the broader distribution of the bias potential  $B$  indicates an (electrostatically) less ordered donor–acceptor interface.

The DR3-based systems exhibit a small additional increase in IQE with increasing IE offset, beyond the steep initial rise. This is most probably caused by incomplete charge separation, as indicated by the IE-offset dependent fraction of geminate recombination (Extended Data Fig. 7 and Supplementary Table 5) possibly due to a larger CT state binding energy with DR3

than with conjugated donor polymers, related to lesser hole delocalization.

To summarize, the interfacial bias potential and associated interfacial energy level bending plays a dual role: it facilitates the dissociation of CT states, but at the same time it reduces the driving force for the exciton-to-CT state conversion. For barrier-less CT state dissociation biases of at least 0.4 eV, that is the CT state Coulomb binding energy, are required.

We demonstrated that ultrafast energy transfer from either small molecule or polymer donors to low-bandgap acceptors in NFA-based solar cells competes with donor to acceptor electron transfer. Energy transfer funnels excitons from donor to acceptor, renders the EA offset virtually unimportant, and leads to a charge generation efficiency exclusively dependent on the IE offset. Furthermore, for small IE offsets, an energy barrier for the acceptor exciton-to-CT state transition exists. This barrier is due to the interfacial energy level bending by the electrostatic fields created by the NFA molecular quadrupole moments. As a result, IE offsets larger than the CT state Coulomb binding energy are required for barrier-less hole transfer from the acceptor to the donor. In fact, IE offsets of 0.5 eV are needed to ensure close-to-unity charge generation efficiency. This sets an intrinsic limit to the minimum energy losses that can be tolerated in NFA-based systems without sacrificing the charge separation efficiency, in other words, ensuring close-to-unity quantum efficiency. It also pinpoints additional system parameters that can be used to further improve the device efficiency. Specifically, the largest fraction of losses that limit the open-circuit voltage is related to the electron-hole Coulomb binding of a CT state and the disorder of the interfacial electrostatic bias potential. Since Coulomb binding of the CT state in NFAs is of the order of 0.4 eV, and close-to unity charge generation efficiency is achieved for 0.5 eV, we can, in principle, further reduce energetic losses by around 0.1 eV, when decreasing the disorder of the electrostatic bias. Further improvements can be achieved by reducing non-geminate (non-radiative) recombination of charges and CT states. Additional improvements will require conceptually new designs that either decrease the Coulomb binding energy of the CT state or generate charges without passing through a CT state intermediate, for example, by tunnelling directly from the excited to the charge-separated state. Apart from the energy losses, the pragmatic way to improve overall OSC efficiency is to increase the absorption coefficient of the donor and acceptor and therefore push the external quantum efficiency (EQE) towards unity, by avoiding carrier recombination losses typical for thicker photoactive layers.

## Online content

Any methods, additional references, Nature Research reporting summaries, source data, extended data, supplementary information, acknowledgements, peer review information; details of author contributions and competing interests; and statements of data and code availability are available at <https://doi.org/10.1038/s41563-020-00835-x>.

Received: 21 September 2019; Accepted: 17 September 2020; Published online: 23 October 2020

## References

1. Yang, C. et al. Effects of energy-level offset between a donor and acceptor on the photovoltaic performance of non-fullerene organic solar cells. *J. Mater. Chem. A* **7**, 18889–18897 (2019).
2. Cha, H. et al. Influence of blend morphology and energetics on charge separation and recombination dynamics in organic solar cells incorporating a nonfullerene acceptor. *Adv. Funct. Mater.* **28**, 1704389 (2018).
3. Kaake, L. G. Towards the organic double heterojunction solar cell. *Chem. Rec.* **19**, 1131–1141 (2019).
4. Menke, S. M., Ran, N. A., Bazan, G. C. & Friend, R. H. Understanding energy loss in organic solar cells: toward a new efficiency regime. *Joule* **2**, 25–35 (2018).

5. Nakano, K. et al. Anatomy of the energetic driving force for charge generation in organic solar cells. *Nat. Commun.* **10**, 2520 (2019).
6. Ward, A. J. et al. The impact of driving force on electron transfer rates in photovoltaic donor-acceptor blends. *Adv. Mater.* **27**, 2496–2500 (2015).
7. Li, Y. et al. Non-fullerene acceptor with low energy loss and high external quantum efficiency: towards high performance polymer solar cells. *J. Mater. Chem. A* **4**, 5890–5897 (2016).
8. Chen, S. et al. A wide-bandgap donor polymer for highly efficient non-fullerene organic solar cells with a small voltage loss. *JACS* **139**, 6298–6301 (2017).
9. Zhang, J. et al. Accurate determination of the minimum HOMO offset for efficient charge generation using organic semiconducting alloys. *Adv. Energy Mater.* **10**, 1903298 (2020).
10. Scharber, M. C. et al. Design rules for donors in bulk-heterojunction solar cells—towards 10% energy-conversion efficiency. *Adv. Mater.* **18**, 789–794 (2006).
11. Ohkita, H. et al. Charge carrier formation in polythiophene/fullerene blend films studied by transient absorption spectroscopy. *JACS* **130**, 3030–3042 (2008).
12. Coffey, D. C. et al. An optimal driving force for converting excitons into free carriers in excitonic solar cells. *J. Phys. Chem. C* **116**, 8916–8923 (2012).
13. Hendriks, K. H., Wijkema, A. S. G., van Franeker, J. J., Wienk, M. M. & Janssen, R. A. J. Dichotomous role of exciting the donor or the acceptor on charge generation in organic solar cells. *JACS* **138**, 10026–10031 (2016).
14. Unger, T. et al. The impact of driving force and temperature on the electron transfer in donor-acceptor blend systems. *J. Phys. Chem. C* **121**, 22739–22752 (2017).
15. Zhou, Z. et al. Subtle molecular tailoring induces significant morphology optimization enabling over 16% efficiency organic solar cells with efficient charge generation. *Adv. Mater.* **32**, 1906324 (2020).
16. Tereshchenko, I. V. et al. The role of semilabile oxygen atoms for intercalation chemistry of the metal-ion battery polyanion cathodes. *JACS* **140**, 3994–4003 (2018).
17. Li, Y. et al. A fused-ring based electron acceptor for efficient non-fullerene polymer solar cells with small HOMO offset. *Nano Energy* **27**, 430–438 (2016).
18. Li, S. et al. Highly efficient fullerene-free organic solar cells operate at near zero highest occupied molecular orbital offsets. *JACS* **141**, 3073–3082 (2019).
19. Yan, C. et al. Non-fullerene acceptors for organic solar cells. *Nat. Rev. Mater.* **3**, 18003 (2018).
20. Chen, S. et al. Efficient nonfullerene organic solar cells with small driving forces for both hole and electron transfer. *Adv. Mater.* **30**, 1804215 (2018).
21. Baran, D. et al. Reduced voltage losses yield 10% efficient fullerene free organic solar cells with >1 V open circuit voltages. *Energy Environ. Sci.* **9**, 3783–3793 (2016).
22. Wan, X., Li, C., Zhang, M. & Chen, Y. Acceptor-donor-acceptor type molecules for high performance organic photovoltaics – chemistry and mechanism. *Chem. Soc. Rev.* **49**, 2828–2842 (2020).
23. Sworakowski, J. How accurate are energies of HOMO and LUMO levels in small-molecule organic semiconductors determined from cyclic voltammetry or optical spectroscopy? *Synth. Met.* **235**, 125–130 (2018).
24. Janssen, R. A. J. & Nelson, J. Factors limiting device efficiency in organic photovoltaics. *Adv. Mater.* **25**, 1847–1858 (2013).
25. Jin, F. et al. Improved charge generation via ultrafast effective hole-transfer in all-polymer photovoltaic blends with large highest occupied molecular orbital (HOMO) energy offset and proper crystal orientation. *Adv. Funct. Mater.* **28**, 1801611 (2018).
26. Aplan, M. P. et al. Revealing the importance of energetic and entropic contributions to the driving force for charge photogeneration. *ACS Appl. Mater. Interfaces* **10**, 39933–39941 (2018).
27. Perdígón-Toro, L. et al. Barrierless free charge generation in the high-performance PM6:Y6 bulk heterojunction non-fullerene solar cell. *Adv. Mater.* **32**, 1906763 (2020).
28. Ramirez, I., Causa, M., Zhong, Y., Banerji, N. & Riede, M. Key tradeoffs limiting the performance of organic photovoltaics. *Adv. Energy Mater.* **8**, 1703551 (2018).
29. Karki, A. et al. Unifying charge generation, recombination, and extraction in low-offset non-fullerene acceptor organic solar cells. *Adv. Energy Mater.* **10**, 2001203 (2020).
30. Gautam, B. R., Younts, R., Carpenter, J., Ade, H. & Gundogdu, K. The role of FRET in non-fullerene organic solar cells: implications for molecular design. *J. Phys. Chem. A* **122**, 3764–3771 (2018).
31. Mohapatra, A. A. et al. Förster resonance energy transfer drives higher efficiency in ternary blend organic solar cells. *ACS Appl. Energy Mater.* **1**, 4874–4882 (2018).
32. Bi, P. et al. Dual Förster resonance energy transfer effects in non-fullerene ternary organic solar cells with the third component embedded in the donor and acceptor. *J. Mater. Chem. A* **5**, 12120–12130 (2017).
33. Karuthedath, S. et al. Impact of fullerene on the photophysics of ternary small molecule organic solar cells. *Adv. Energy Mater.* **9**, 1901443 (2019).
34. Zhong, Y. et al. Sub-picosecond charge-transfer at near-zero driving force in polymer:non-fullerene acceptor blends and bilayers. *Nat. Commun.* **11**, 833 (2020).
35. Liang, R.-Z. et al. Carrier transport and recombination in efficient “All-Small-Molecule” solar cells with the nonfullerene acceptor IDTBR. *Adv. Energy Mater.* **8**, 1800264 (2018).
36. Alamoudi, M. A. et al. Impact of nonfullerene acceptor core structure on the photophysics and efficiency of polymer solar cells. *ACS Energy Lett.* **3**, 802–811 (2018).
37. Yuan, J. et al. Single-junction organic solar cell with over 15% efficiency using fused-ring acceptor with electron-deficient core. *Joule* **3**, 1140–1151 (2019).
38. Gao, F. A new acceptor for highly efficient organic solar cells. *Joule* **3**, 908–909 (2019).
39. Yoshida, H. Note: low energy inverse photoemission spectroscopy apparatus. *Rev. Sci. Instrum.* **85**, 16101 (2014).
40. Yao, H. et al. Design and synthesis of a low bandgap small molecule acceptor for efficient polymer solar cells. *Adv. Mater.* **28**, 8283–8287 (2016).
41. Huang, J.-S. et al. Polymer bulk heterojunction solar cells employing Förster resonance energy transfer. *Nat. Photon* **7**, 479–485 (2013).
42. Sapsford, K. E., Berti, L. & Medintz, I. L. Materials for fluorescence resonance energy transfer analysis: beyond traditional donor-acceptor combinations. *Angew. Chem. (Int. ed. Engl.)* **45**, 4562–4589 (2006).
43. Poelking, C. & Andrienko, D. Design rules for organic donor-acceptor heterojunctions: pathway for charge splitting and detrapping. *JACS* **137**, 6320–6326 (2015).
44. Poelking, C. et al. Impact of mesoscale order on open-circuit voltage in organic solar cells. *Nat. Mater.* **14**, 434–439 (2015).
45. Castet, F., D’Avino, G., Muccioli, L., Cornil, J. & Beljonne, D. Charge separation energetics at organic heterojunctions: on the role of structural and electrostatic disorder. *Phys. Chem. Chem. Phys.* **16**, 20279–20290 (2014).
46. Schwarze, M. et al. Band structure engineering in organic semiconductors. *Science* **352**, 1446–1449 (2016).
47. D’Avino, G. et al. Electrostatic phenomena in organic semiconductors: fundamentals and implications for photovoltaics. *J. Phys. Condens. Matter* **28**, 433002 (2016).
48. Schwarze, M. et al. Impact of molecular quadrupole moments on the energy levels at organic heterojunctions. *Nat. Commun.* **10**, 2466 (2019).
49. Sousa, L. E., Coropceanu, V., da Silva Filho, D. A. & Sini, G. On the physical origins of charge separation at donor-acceptor interfaces in organic solar cells: energy bending versus energy disorder. *Adv. Theory Simul.* **3**, 1900230 (2020).

**Publisher's note** Springer Nature remains neutral with regard to jurisdictional claims in published maps and institutional affiliations.

© The Author(s), under exclusive licence to Springer Nature Limited 2020

## Methods

**Materials.** PBDB-T-2F, IT-4F, Y6, IEICO-4F were purchased from Solarmer Materials Inc. DR3TBDTT (DR3), PTB7-Th, ITIC, ICC6 (IDIC), BT-CIC, IT-4Cl, IEICO and Phen-NaDPO were purchased from 1-Material Inc. IDTTBM<sup>50</sup> and O-IDTBR<sup>51</sup> were synthesized at KAUST. PC<sub>71</sub>BM was obtained from Solenne BV, PEDOT:PSS from Heraeus and PBDB-T-SF and PFN-Br from Organtec Ltd. Chlorobenzene anhydrous 99.8%, carbon disulfide anhydrous ≥99% and 1,8-diiodooctane 98% were purchased from Sigma-Aldrich, chloroform from VWR, 1-chloronaphthalene from Fluka and dimethyldisulfide 99% from Alfa Aesar. All materials were used as received.

Full material names: IT-4Cl, 3,9-*bis*(2-methylene-((3-(1,1-dicyanomethylene)-chloro)-indanone))-5,5,11,11-tetrakis(4-hexylphenyl)-dithieno[2,3-d':2',3'-d']-s-indaceno[1,2-b:5,6-b']dithiophene; IT-4F, 3,9-*bis*(2-methylene-((3-(1,1-dicyanomethylene)-6,7-difluoro)-indanone))-5,5,11,11-tetrakis(4-hexylphenyl)-dithieno[2,3-d':2',3'-d']-s-indaceno[1,2-b:5,6-b']dithiophene; ITIC, 3,9-*bis*(2-methylene-((3-(1,1-dicyanomethylene)-indanone))-5,5,11,11-tetrakis(4-hexylphenyl)-dithieno[2,3-d':2',3'-d']-s-indaceno[1,2-b:5,6-b']dithiophene; Y6, (2,20-((2Z,20Z)-((12,13-*bis*(2-ethylhexyl)-3,9-diundecyl-12,13-dihydro-[1,2,5]thiadiazolo[3,4-*e*]thieno[2,30':4',50]thieno[20,30:4,5]pyrrolo[3,2-*g*]thieno[20,30:4,5]thieno[3,2-*b*]indole-2,10-diyl)bis(methanylylidene))*bis*(5,6-difluoro-3-oxo-2,3-dihydro-1*H*-indene-2,1-diylidene))dimalononitrile). ICC6: indacenodithiophene end capped with 1,1-dicyanomethylene-3-indanone; IEICO-4F, 2,2'-[[4,4,9,9-tetrakis(4-hexylphenyl)-4,9-dihydro-s-indaceno[1,2-b:5,6-b']dithiophene-2,7-diyl]bis[[4-(2-ethylhexyl)oxy]-5,2-thiophenediyl]methylidene(5,6-difluoro-3-oxo-1*H*-indene-2,1(3*H*)-diylidene)]*bis*[propanedinitrile]; O-IDTBR, 5,5'-[[4,9-dihydro-4,4,9,9-tetraoctyl-s-indaceno[1,2-b:5,6-b']dithiophene-2,7-diyl]bis(2,1,3-benzothiazolidone-7,4-diylmethylidene)]*bis*[3-ethyl-2-thioxo-4-thiazolidinone]; BT-CIC, 4,4,10,10-tetrakis(4-hexylphenyl)-5,11-(2-ethylhexyloxy)-4,10-dihydrodithienyl[1,2-b:4,5b']benzodithiophene-2,8-diyl)*bis*(2-(3-oxo-2,3-dihydroindene-5,6-dichloro-1-ylidene)malononitrile); IEICO, 2,2'-((2Z,2'Z)-((5,5'-(4,4,9,9-tetrakis(4-hexylphenyl)-4,9-dihydro-s-indaceno[1,2-b:5,6-b']dithiophene-2,7-diyl)bis(4-((2-ethylhexyl)-oxy)thiophene-5,2-diyl)bis(methanylylidene))*bis*(3-oxo-2,3-dihydro-1*H*-indene-2,1-diylidene))dimalononitrile; IDTTBM, indacenodithienothienophene 2-(benzo[*c*][1,2,5]thiadiazol-4-ylmethylene)malononitrile; PC<sub>71</sub>BM, [6,6]-phenyl-C71-butyric acid methyl ester; Phen-NaDPO, ((2-(1,10-phenanthroline-3-yl)naphth-6-yl)diphenylphosphine oxide); PEDOT:PSS, poly(3,4-ethylenedioxythiophene):poly(styrenesulfonate); PFN-Br, Poly(9,9-*bis*(3'-(*N,N*-dimethyl)-*N*-ethylammonium *m*-propyl-2,7-fluorene)-alt-2,7-(9,9-dioctylfluorene))dibromide; PBDB-T-2F, poly[(2,6-(4,8-*bis*(5-(2-ethylhexyl)-3-fluoro)thiophen-2-yl)-benzo[1,2-b:4,5-b']dithiophene))-alt-(5,5-(1',3'-di-2-thienyl-5',7'-*bis*(2-ethylhexyl)benzo[1,2'-c:4',5'-c']dithiophene-4,8-dione)); PBDB-T-SF, poly[(2,6-(4,8-*bis*(5-(2-ethylhexylthio)-4-fluorothiophen-2-yl)-benzo[1,2-b:4,5-b']dithiophene))-alt-(5,5-(1',3'-di-2-thienyl-5',7'-*bis*(2-ethylhexyl)benzo[1,2'-c:4',5'-c']dithiophene-4,8-dione)); PTB7-Th, poly[(2,6'-4,8-di(5-ethylhexylthienyl)benzo[1,2-b:3,3-b']dithiophene)) and DR3, (5Z,5'E)-5,5'-((4,8-*bis*(5-(2-ethylhexyl)thiophen-2-yl)benzo[1,2-b:4,5-b']dithiophene-2,6-diyl)bis(3,3'-diocetyl-2,2':5',2"-terthiophene)-5",5-diyl)bis(methanylylidene))*bis*(3-ethyl-2-thioxothiazolidin-4-one).

**Thin-film and device preparation.** Organic photovoltaic cells were fabricated using indium-tin-oxide (ITO)-coated glass substrate with a sheet resistance of 10 Ω sq<sup>-1</sup>. Substrates were cleaned by sequential ultrasonication in dilute Extran 300 detergent solution, deionized water, acetone and isopropyl alcohol for 10 min each. The substrates were then subjected to a UV-ozone treatment for 10 min. For normal architecture solar cells, a thin layer (≈30 nm) of PEDOT:PSS was spin-coated onto the UV-treated substrates and then dried on a heating plate at 150 °C for 10 min. For inverted solar cells, zinc oxide (ZnO) sol-gel was spin-coated on cleaned glass-ITO substrates with a spin speed of 4,000 r.p.m. for 30 s, yielding a thickness of around 20 nm. The as-cast films were then thermally annealed in air at 150 °C for 10 min and allowed to cool down to room temperature. Active layers were obtained by dissolving donor and acceptor in organic solvents (chloroform or chlorobenzene) inside the glovebox. The as-prepared solutions were stirred for at least 1 h at 40–50 °C before being cast on the substrates. The active layers were spin-cast from the solutions at 50 °C for 45 s, using a programmable spin-coater from Specialty Coating Systems (Model G3P-8). The active layers were then annealed (solvent vapour annealed for all-small molecule cells and thermally annealed for polymer-based cells). For normal architecture cells, a layer of 5 nm of Phen-NaDPO (or PFN-Br for polymer-based cells) as the electron-transport layer was spun from methanol solution (0.5 mg ml<sup>-1</sup>) on top of the BHJ layer. Next, the samples were placed in a thermal evaporator for evaporation of a 100-nm-thick layer of aluminium evaporated at 5 Å s<sup>-1</sup> at a pressure of less than 2 × 10<sup>-6</sup> Torr. For inverted architecture devices, 7 nm of molybdenum(VI) oxide MoO<sub>3</sub> (Alfa) and 100 nm of Ag (Kurt Lesker) were evaporated. The effective area of the tested solar cells is 0.1 cm<sup>2</sup>. This effective area was determined from the layout of ITO substrate and top contact mask. Details of active-layer preparation and optimization are given in Supplementary Tables 3 and 4.

**Device characterization.** *J-V* characteristics of solar cells were measured in a nitrogen-filled glovebox. Solar cells were illuminated with light from an Oriol

Sol3A Class AAA solar simulator calibrated to 1 sun, AM1.5G, with a KG-5 silicon reference cell certified by Newport. A Keithley 2400 source meter was used to measure the *J-V* curves in the reverse direction, that is, from positive to negative bias with a dwell time of 10 ms. For each *J-V* curve 100 data points were collected. The solar cells' EQE was measured with a commercial setup (PV Measurement Inc.) at zero bias. Solar cells were illuminated with light supplied from a Xenon arc lamp in combination with a dual-grating monochromator. For each wavelength, the number of incident photons was calculated using a calibrated silicon photodiode. Calibration was performed by The National Institute of Standards and Technology. The IQE of organic photovoltaic devices was calculated using: IQE(%) = EQE(%) / (100% - reflectance(%) - parasitic absorption(%)). The reflectance spectra were measured in an integrating sphere using the same EQE setup, while the parasitic absorption spectra were obtained by transfer matrix modelling of the device stack.

**UPS and LE-IPES spectroscopy.** The substrate for film deposition was Au (100 nm)/Cr (10 nm)/Si (*n*-type), with the Au and Cr evaporated and sputtered within an Angstrom evaporation/sputter tool, respectively. Solutions of 2–5 mg ml<sup>-1</sup> in chloroform were prepared and stirred overnight in a glovebox and then spin-coated (5,000 r.p.m. for 1 min) onto an Ar<sup>+</sup> ion sputtered Au substrate and then transferred to ultra-high vacuum for analysis. The organic small molecule/polymer film thickness was 10–20 nm.

UPS was performed with a vacuum UV He (1) discharge line 21.22 eV (focus) and a Sphera II EAC 125 7-channeltron electron analyser<sup>52</sup>. A small component of roughly 2% β (23.09 eV) was present. The sample was positioned at 0° with respect to the analyser-to-sample plane. Fermi level calibration was performed using an Ar<sup>+</sup> sputtered clean metallic Ag foil in electrical contact to the manipulator holding the sample in contact with the electron analyser. During UPS a bias of -9.97 eV was applied to observe the secondary electron cut-off. Subsequent measurements were made in electrical contact with thin films to prevent surface charging. UPS Scans were conducted from low to high kinetic energy at a constant analyser pass energy of 10 eV and subsequent scans were carefully monitored to detect beam-induced degradation or evidence of charging.

As shown in the Extended Data Figs. 1a, 2a and 3a, the low kinetic energy secondary electron cut-off was used to determine the sample work function WF<sup>53</sup>. A linear extrapolation to the baseline allows approximate determination using the following equation:

$$KEe = h\nu - \phi - EB = 0$$

where KEe is the photoelectron kinetic energy (equal to 0 at secondary electron cut-off),  $h\nu$  is the excitation energy He(1) 21.22 eV, EB is the binding energy relative to the Fermi energy of a sputter-cleaned Ag foil, determined in a separate measurement and  $\phi$  the work function to the local vacuum level. The estimated precision and spectra reproducibility is ±0.05 eV.

An in-house built ultra-high vacuum LE-IPES setup was used following closely a design outlined by Yoshida<sup>54</sup> that was also developed from a previous design<sup>54</sup>. This operates in the Bremsstrahlung isochromatic mode. In brief, an incident electron beam (dispersion of 0.25–0.5 eV) is directed at 0° with respect to the sample plane, and the electron energy is swept slowly. The outgoing light from the surface was collected by placing an external focusing lens and an internal vacuum collimating lens with a detector and all further stray light shielded. This was conducted with a low-energy electron source (Staib) operating in the range of 20–30 eV energy (BaO cathode Heatwaves), with a retarding bias of +20 V applied to the sample in good electrical contact. As stated, the photons were collected outside of vacuum by a solid-state PMT detector (Hamamatsu R585) (0.5–1 h, integration time ~10–20 s, 200 data points), facing the sample within a narrow wavelength window using a bandpass filter of 280 nm (Semrock) (10-nm width). This measurement was performed consecutively without either exposure to Al Kα X-ray 1,486.6 eV for X-ray photoelectron analysis or re-exposure of the surface to ambient atmosphere in a base pressure of 10<sup>-9</sup> mbar to accurately join with UPS spectra. More information can be found in the Supplementary Information Section I.

**Optical bandgap from intersection of steady-state absorption and emission spectra.** The thin-film UV-visible (UV-vis) light absorption and PL spectra were measured with a Cary 5000 spectrophotometer and a Fluoromax-4 spectrofluorometer from Horiba Scientific, respectively.

**TEM.** TEM studies in combination with EELS were performed on a Thermo Fischer Titan 80–300 TEM equipped with an electron monochromator and a Gatan Imaging Filter Quantum 966. Details of the data analysis can be found in the Supplementary Information Section V.

**TA spectroscopy.** TA pump-probe measurements were carried out with a home-built setup described in ref. 55. The setup description is reproduced here for completeness. Two different configurations of the setup were used for either short delay, namely 100 fs to 8 ns experiments, or long delay, namely 1 ns to 300 μs delays, as described below.

The output of a titanium:sapphire amplifier (Coherent LEGEND DUO, 4.5 mJ, 3 kHz, 100 fs) was split into three beams (2, 1 and 1.5 mJ). Two of them

separately pumped two optical parametric amplifiers (Light Conversion TOPAS Prime). TOPAS 1 generates tuneable pump pulses, while TOPAS 2 generates signal (1,300 nm) and idler (2,000 nm). A fraction of the output signal of the titanium:sapphire amplifier was focused into a c-cut 3-mm-thick sapphire window, thereby generating a white-light supercontinuum from 500 to 1,600 nm. For short delay TA measurements, we used the output of TOPAS 1 as pump pulses, while the probe pathway length to the sample was kept constant at approximately 5 m between the output of TOPAS 1 and the sample. The pump pathway length was varied between 5.12 and 2.6 m with a broadband retroreflector mounted on an automated mechanical delay stage (Newport linear stage IMS600CCHA controlled by a Newport X-ray photoelectron motion controller), thereby generating delays between pump and probe from  $-400$  ps to 8 ns. Alternatively, for probing TA further in the blue to violet range of light, we used the 1,300 nm (signal) output of TOPAS 2 to produce a white-light supercontinuum from 350 to 1,100 nm from a  $\text{CaF}_2$  crystal kept under constant motion parallel to the focal plan of the seed beam to avoid damage.

For the 1 ns to 300  $\mu\text{s}$  delay (long delay) TA measurement, the same probe white-light supercontinuum was used as for the 100 fs to 8 ns delays. Here the excitation pulse was provided by an actively Q-switched Nd:YVO<sub>4</sub> laser (InnoLas piccolo AOT) frequency-doubled, providing pulses at 532 nm. The pump laser was triggered by an electronic delay generator (Stanford Research Systems DG535) itself triggered by the transistor–transistor logic sync from the Legend DUO, allowing control of the delay between pump and probe with a jitter of roughly 100 ps.

Pump and probe beams were both focused on the sample, which was kept under a dynamic vacuum of  $<10^{-5}$  mbar generated by a turbo-molecular pump (Pfeiffer Cube). The transmitted fraction of the white light was guided to a custom-made prism spectrograph (Entwicklungsbüro Stresing), where it was dispersed by a prism onto a 512-pixel NMOS (N-type metal-oxide-semiconductor) linear image sensor (Hamamatsu G11608-512DA). The probe pulse repetition rate was 3 kHz, while the excitation pulses were mechanically chopped to 1.5 kHz (100 fs to 8 ns delays). Adjacent diode readings corresponding to the transmission of the sample with and without previous excitation were used to calculate  $\Delta T/T$ . Measurements were averaged over several thousand probes to obtain a reasonable signal-to-noise ratio. The chirp induced by the remaining transmissive optics was corrected with a home-built MATLAB code. The delay at which pump and probe arrive simultaneously on the sample (referred as zero time) was determined from the point of maximum positive slope of the TA signal rise for each wavelength, which is expected to correspond to the maximum of the pump laser pulse.

**TRPL spectroscopy.** For TRPL experiments, samples (films on quartz substrates unless stated) were excited with the wavelength-tuneable output of an optical parametric oscillator (Radiantis Inspire HF-100), itself pumped by the fundamental of a Ti:Sa fs-oscillator (Spectra Physics MaiTai eHP) and a Modelocked Ti:Sa (Chameleon Ultra I from Coherent) at 820 nm. Typical pulse energies were in the range of several nano-joules (nJ). The samples were kept in a nitrogen-filled custom-made sample chamber. The PL of the samples was collected by an optical telescope (consisting of two plano-convex lenses), focused on the slit of a spectrograph (Princeton Instrument Spectra Pro SP2300) and detected with a Streak Camera (Hamamatsu C10910) system with a temporal resolution of 1.4 ps. The data were acquired in photon counting mode using the Streak Camera software (HPDTA) and exported to Origin Pro 2019 for further analysis. The TRPL decays were analysed with a sum of exponentials, and when more than one exponential was found, the amplitude weighted average lifetime was calculated.

**FRET radii and rates.** Transmittance and reflectance spectra for extinction coefficients were measured with a PerkinElmer LAMBDA 950 UV–vis/near-infrared spectrophotometer equipped with a 150-mm InGaAs integrating sphere and the spectra for PL quantum yields (PLQYs) were measured with a FLS920-s Fluorescence Spectrometer by Edinburgh Instruments equipped with a 120-mm integrating sphere. The details of the FRET radii calculations can be found in the Supplementary Information Section VI.

**Sensitive EQE and electroluminescence spectroscopy.** The high-dynamic range EQE spectra were collected at short-circuit conditions using focused monochromatic illumination from a Xenon arc lamp combined with a monochromator. The light was modulated by an optical chopper at 275 Hz. The device output current was demodulated using a Stanford Instruments SR 830 lock-in amplifier for each incident photon energy. The lamp intensity was calibrated with Ge and Si photo-diodes.

The electroluminescence setup has been described in ref. <sup>56</sup>, description reproduced here: the measurements were carried out on devices (active area of 0.1 cm<sup>2</sup>) biased with d.c. voltages (Keithley 2420) similar to or lower than  $V_{\text{OC}}$  at 1 sun illumination. The emission was collected by a collimator inside a nitrogen-filled glovebox and guided to a spectrograph (Princeton Instruments SP2300) by an optical fibre. The spectrometer was equipped with a cooled Si CCD (Princeton Instruments PIX100BRX) and cooled InGaAs (Princeton Instruments PYR1024) camera. The system was wavelength calibrated with a Ne/Ar calibration light source (Princeton Instruments IntelliCal). The visible and infrared spectra were assembled at the 933 nm where they share the same relative sensitivity.

**Computer simulations.** Solid-state IEs were evaluated in a perturbative way, starting from the gas-phase quantum-chemical calculations (B3LYP/6-311g(d,p) level as implemented in the GAUSSIAN 09 package<sup>57</sup>) and then taking into account solid-state contribution as a perturbation, where electrostatic and induction energies are the first- and second-order corrections. These contributions to site energies were calculated self-consistently using the Thole model<sup>58,59</sup> using atomic polarizabilities and distributed multipoles using the GDMA program<sup>60</sup> for a cation and a neutral molecule. This approach, in combination with an aperiodic inclusion of charges to a neutral periodic morphology, is available in the VOTCA-CTP package<sup>61,62</sup>. Further details are given in the Supplementary Information.

**Reporting Summary.** Further information on research design is available in the Nature Research Reporting Summary linked to this article.

## Data availability

The datasets generated and analysed during this study and presented in this article are available online at <https://doi.org/10.6084/m9.figshare.c.5110076.v1>.

## Code availability

The codes or algorithms used to analyse the data reported in this study are available from the corresponding authors upon reasonable request.

## References

- Liang, R.-Z. et al. Additive-morphology interplay and loss channels in 'All-Small-Molecule' bulk-heterojunction (BHJ) solar cells with the nonfullerene acceptor IDTTBM. *Adv. Funct. Mater.* **28**, 1705464 (2018).
- Holliday, S. et al. High-efficiency and air-stable P3HT-based polymer solar cells with a new non-fullerene acceptor. *Nat. Commun.* **7**, 11585 (2016).
- Yang, J.-P. et al. Origin and role of gap states in organic semiconductor studied by UPS: as the nature of organic molecular crystals. *J. Phys. D. Appl. Phys.* **50**, 423002 (2017).
- Kahn, A. Fermi level, work function and vacuum level. *Mater. Horiz.* **3**, 7–10 (2016).
- Yoshida, H. Near-ultraviolet inverse photoemission spectroscopy using ultra-low energy electrons. *Chem. Phys. Lett.* **539–540**, 180–185 (2012).
- Karuthedath, S. et al. Thermal annealing reduces geminate recombination in TQ1:N2200 all-polymer solar cells. *J. Mater. Chem. A* **6**, 7428–7438 (2018).
- Babics, M. et al. Negligible energyloss during charge generation in small-molecule/fullerene bulk-heterojunctionsolar cells leads to open-circuit voltage over 1.10 V. *ACS Appl. Energy Mater.* **2**, 2717–2722 (2019). 4.
- Frisch, M. J. et al. Gaussian 09 (Gaussian Inc., 2016).
- Thole, B. T. Molecular polarizabilities calculated with a modified dipole interaction. *Chem. Phys.* **59**, 341–350 (1981).
- van Duijnen, P. T. & Swart, M. Molecular and atomic polarizabilities: Thole's model revisited. *J. Phys. Chem. A* **102**, 2399–2407 (1998).
- Stone, A. J. Distributed multipole analysis: stability for large basis sets. *J. Chem. Theory Comput.* **1**, 1128–1132 (2005).
- Rühle, V. et al. Microscopic simulations of charge transport in disordered organic semiconductors. *J. Chem. Theory Comput.* **7**, 3335–3345 (2011).
- Poelking, C. & Andrienko, D. Long-range embedding of molecular ions and excitations in a polarizable molecular environment. *J. Chem. Theory Comput.* **12**, 4516–4523 (2016).

## Acknowledgements

This publication is based on work supported by the KAUST Office of Sponsored Research (OSR) under award nos. OSR-2018-CARF/CCF-3079 and OSR-CRG2018-3746. D.A. acknowledges funding from the BMBF grant InterPhase and MESOMERIE (grant nos. FKZ 13N13661, FKZ 13N13656) and the European Union Horizon 2020 research and innovation program 'Widening materials models' under grant agreement no. 646259 (MOSTOPHOS). D.A. also acknowledges the KAUST PSE Division for hosting his sabbatical in the framework of the Division's Visiting Faculty program. A.M. acknowledges funding from the European Union's Horizon 2020 research and innovation program under the Marie Skłodowska-Curie grant agreement no. 844655 (SMOLAC). We thank L. Sinatra of KAUST and Quantum Solutions LLC for assisting with the PLQY measurements. G.T.H. acknowledges K. Graham and A. Amassian (and previous group members including M. Tietze and G.O.N. Ndjawa) for having designed and installed and worked on the IPES setup. In particular, G.T.H. acknowledges K. Graham's kind assistance during the reconfiguration and optimization of the IPES setup, as well as U. Sharif for technical assistance.

## Author contributions

S.K. performed the transient spectroscopy experiments, data analysis and prepared the first draft of the manuscript. J.G. conceived the study, analysed the transient and steady-state spectroscopic experiments, carried out the FRET calculations and contributed to the manuscript. Y.F. performed the DR3, PTB7-Th and PBDB-T-2F-based solar cell device preparation and characterization, and the ellipsometry measurements and analysis. N.C. prepared and characterized PBDB-T-SF-based devices

and prepared thin-film blends for TRPL experiments. C.S.P.D.C. prepared samples and characterized the steady-state absorption of thin films, PLQY and PL quenching in DR3, PTB7-Th and PBDB-T-2F-based blends via TRPL. G.T.H. performed the UPS and LE-IPES experiments and data analysis. J.I.K. provided steady-state absorption, PL and TRPL data of PBDB-T-SF-based blends. A.M. calculated the solid-state IEs, EAs and bias potentials. W.L. performed quantum-chemical calculations of donor-acceptor dimers. A.H.B. and T.A.D.P. determined the CT state energies from electroluminescence spectra. R.-Z.L. prepared DR3-based devices and characterized their performance. W.Z. synthesized the O-IDTBR acceptor. Y.L. prepared thin films for steady-state characterization. D.H.A. performed thin-film imaging and EELS analysis. E.A. contributed to the development and maintenance of the ultrafast laser spectroscopy setups. S.H.K.P. determined the IQE of PTB7-Th-based devices. A.S. determined the IE and EA of IEICO-4F and IT-4F by UPS and LE-IPES, respectively. P.M.B. supervised the device preparation of DR3-based solar cells and synthesis of IDTTBM used in this work. S.D.W. oversaw the UPS/LE-IPES experiments and data analysis. I.M. supervised the synthesis of O-IDTBR used in this work. T.D.A. supervised the PBDB-T-2F, and some of the R3 and PTB7-Th donor device preparation and characterization. D.B. supervised some of the PTB7-Th donor device preparation and

characterization. D.A. supervised the computational part of the work, conceived the model describing the energy level bending and contributed to the manuscript. F.L. conceived the study and supervised the steady-state and transient optical spectroscopy experiments and data analysis, as well as the PBDB-T-SF donor device preparation and characterization and contributed to the manuscript. All authors contributed to the revision of the final version of the manuscript.

### Competing interests

The authors declare no competing interests.

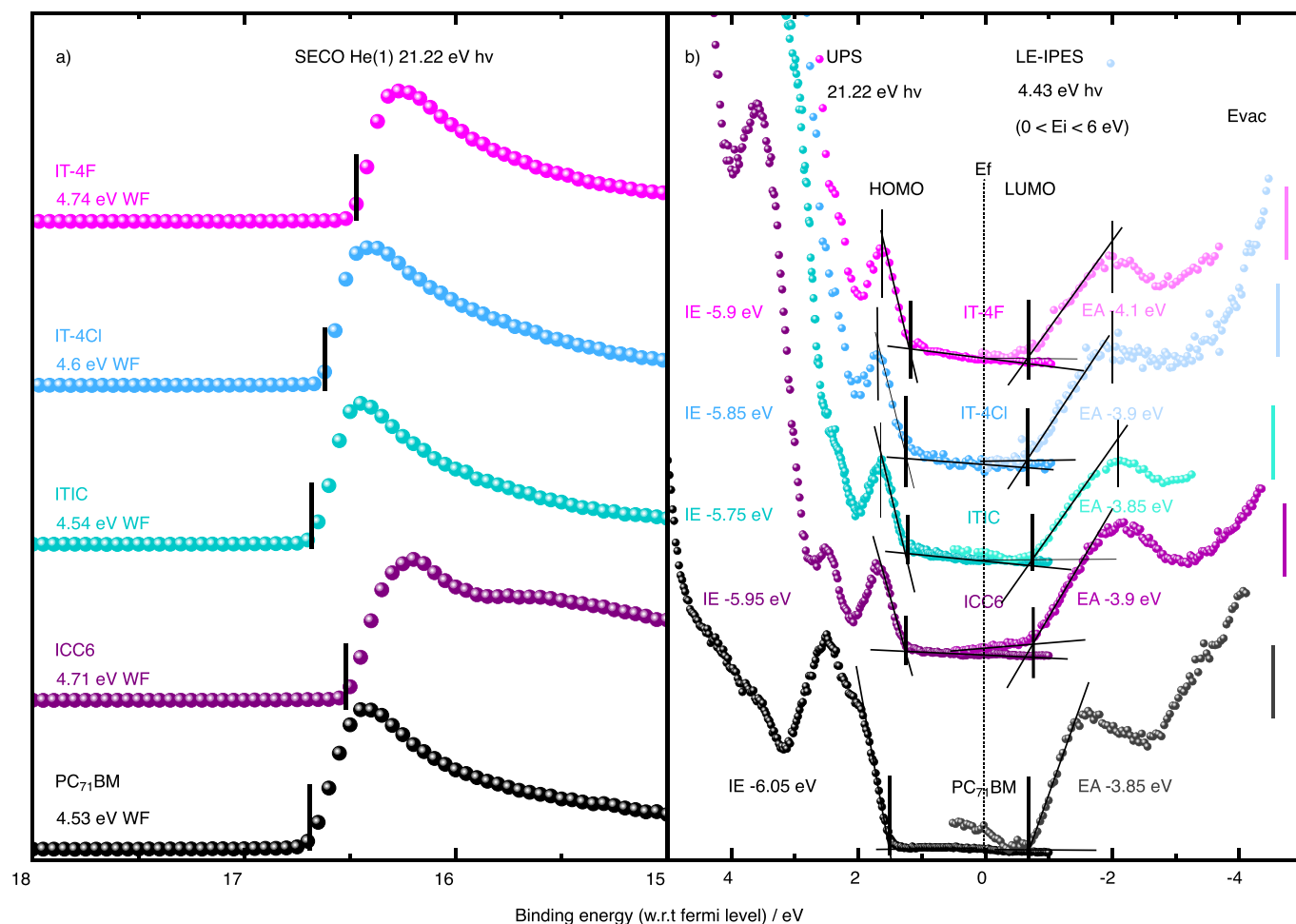
### Additional information

**Extended data** is available for this paper at <https://doi.org/10.1038/s41563-020-00835-x>.

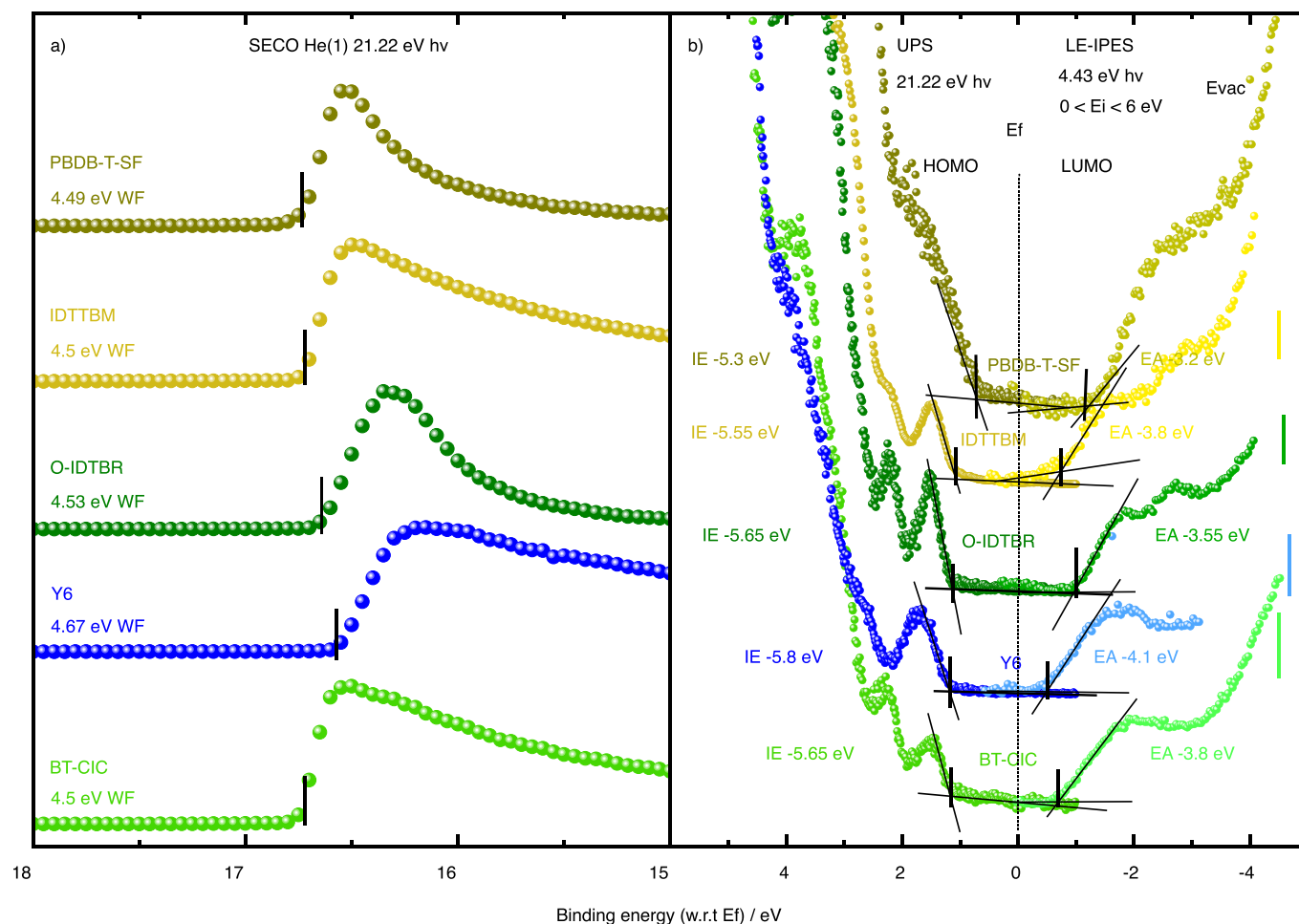
**Supplementary information** is available for this paper at <https://doi.org/10.1038/s41563-020-00835-x>.

**Correspondence and requests for materials** should be addressed to D.A. or F.L.

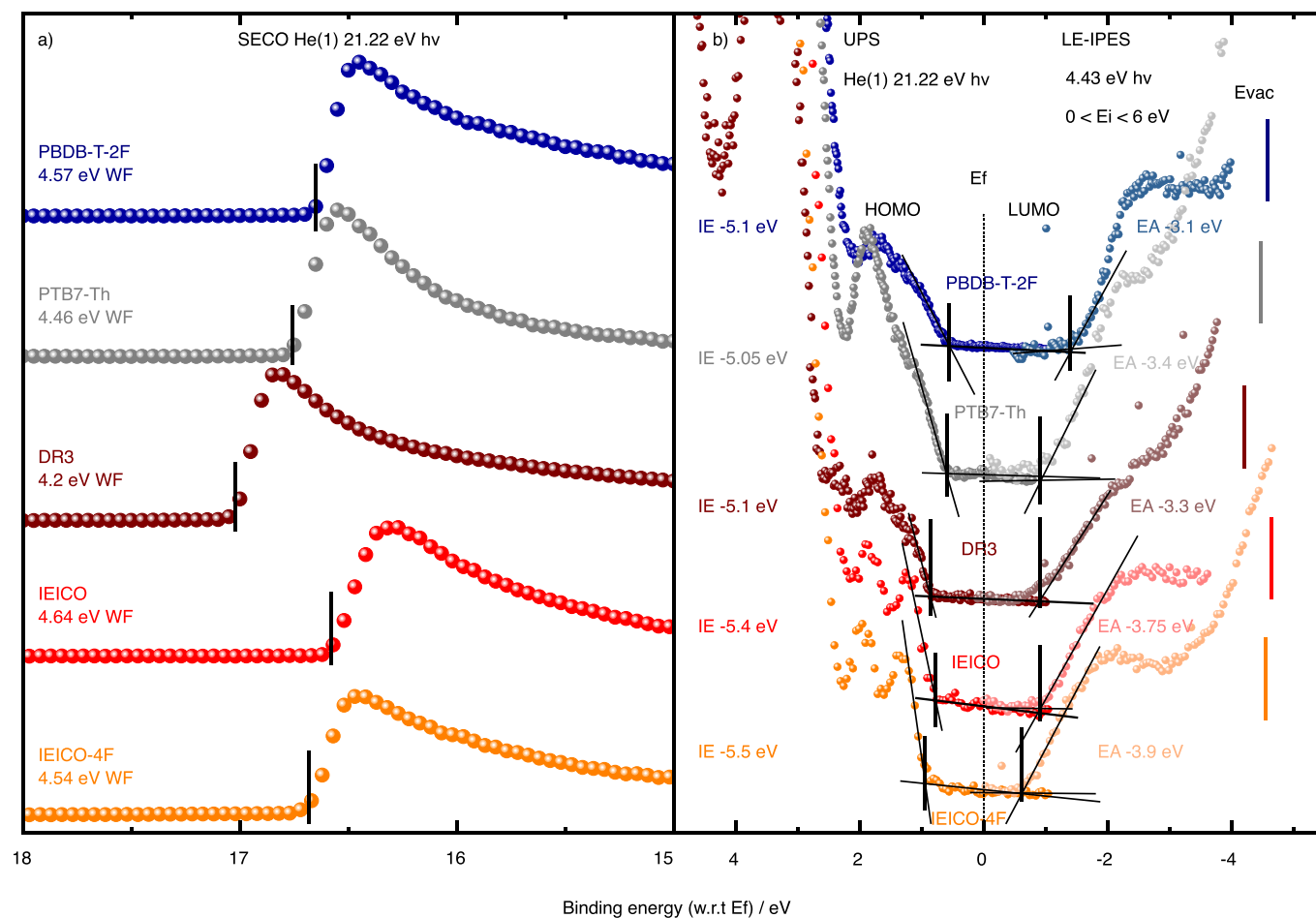
**Reprints and permissions information** is available at [www.nature.com/reprints](http://www.nature.com/reprints).



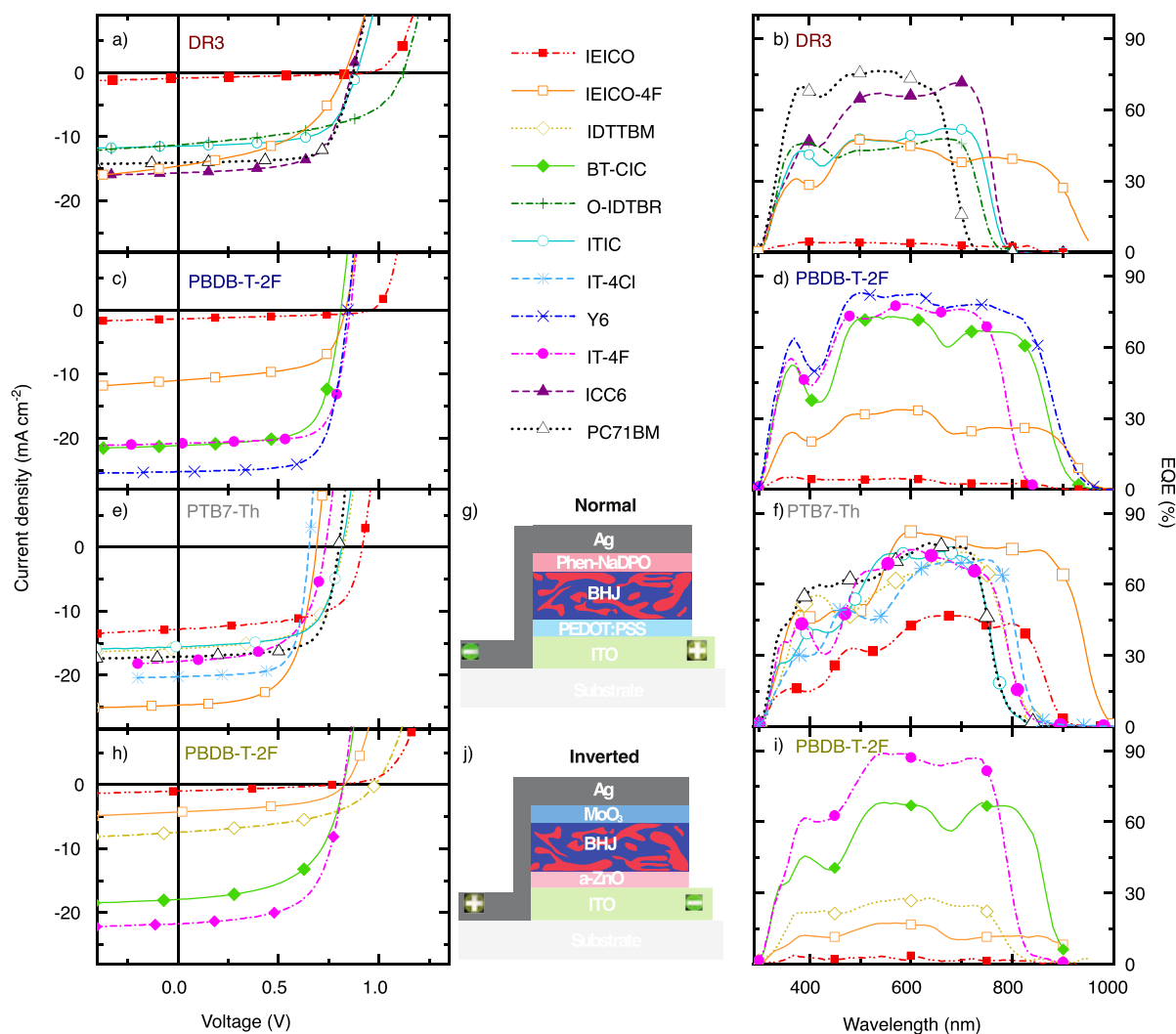
**Extended Data Fig. 1 | UPS and LE-IPES spectra of IT-4F, IT-4Cl, ITIC, ICC6 and PCBM.** UPS and LE-IPES spectra of IT-4F, IT-4Cl, ITIC, ICC6, and PC<sub>71</sub>BM thin films on evaporated Au100nm/Cr10nm/n-type Si(100). **a)** SECO region normalized to the SEC peak height and offset with work function (WF) values labelled. **b)** UPS (left) and LE-IPES (right) spectra displayed with respect to the Fermi level at 0. The intersection between the flat baseline and tangent of the respective frontier orbitals band defines here the HOMO and LUMO level and IE and EA with respect to vacuum. These are identified by black vertical lines and value labeled. The respective vacuum levels are displayed by the vertical lines.



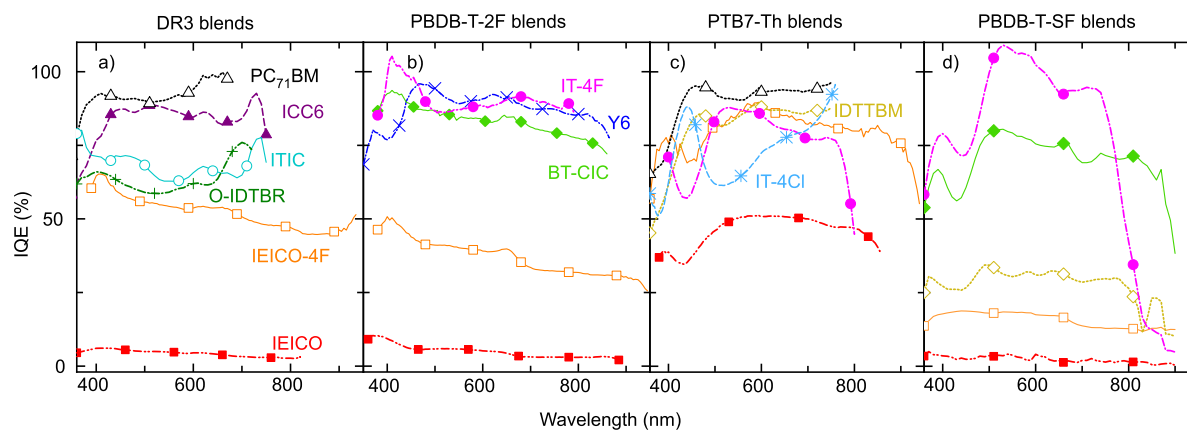
**Extended Data Fig. 2 | UPS and LE-IPES spectra of PBDB-T-SF, IDTTBM, O-IDTBR, Y6 and BT-CIC.** UPS and LE-IPES spectra of PBDB-T-SF, IDTTBM, O-IDTBR, Y6, and BT-CIC thin films on evaporated Au100nm/Cr10nm/n-type Si(100). **a)** SECO region normalized to the SEC peak height and offset with work function (WF) values labeled. **b)** UPS (left) and LE-IPES (right) spectra displayed with respect to the Fermi level at 0. The intersection between the flat baseline and tangent of the respective frontier orbitals band defines here the HOMO and LUMO level and IE and EA with respect to vacuum. These are identified by black vertical lines and value labeled. The respective vacuum levels are displayed by the vertical lines.



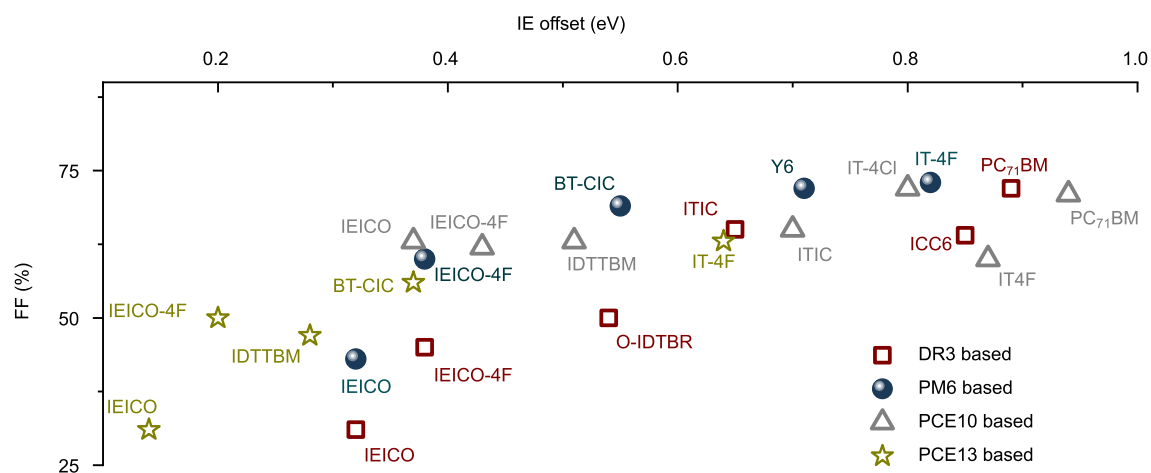
**Extended Data Fig. 3 | UPS and LE-IPES spectra of PBDB-T-2F, PTB7-Th, DR3, IEICO and IEICO-4F.** UPS and LE-IPES spectra of PBDB-T-2F, PTB7-Th, DR3, IEICO, and IEICO-4F thin films on evaporated Au100nm/Cr10nm/n-type Si(100). **a)** SECO region normalized to the SEC peak height and offset with work function (WF) values labeled. **b)** UPS (left) and LE-IPES (right) spectra displayed with respect to the Fermi level (0 eV). Vertical marks identify the estimated HOMO and LUMO energetic values (IE and EA with respect to vacuum) with lines used in the linear extrapolation to baseline shown. Vertical lines identify the vacuum energy (Evac). (UPS photoelectron intensity (a.u.), IPES PMT photon intensity (a.u)).



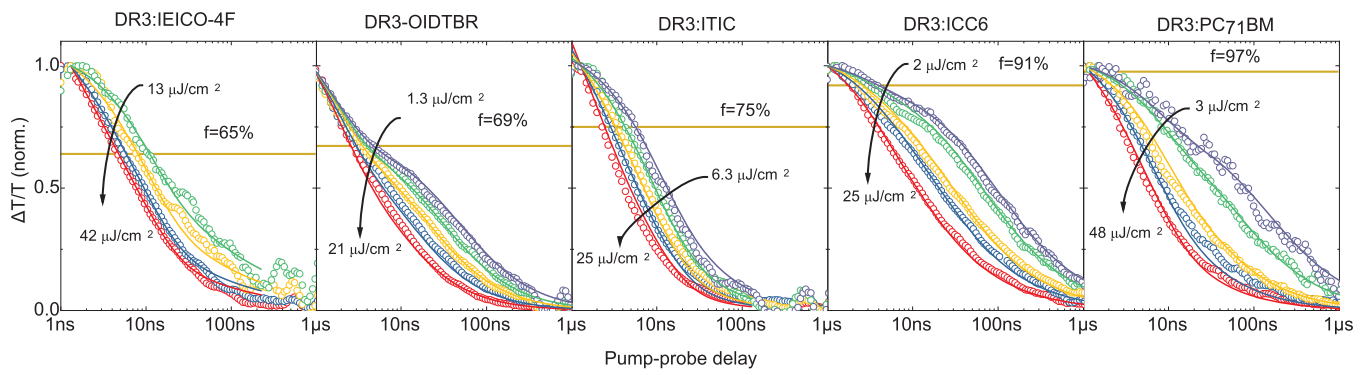
**Extended Data Fig. 4 | J-V curves and EQE spectra of DR3-, PBDB-T-2F-, PTB7-Th- and PBDB-T-SF-based devices.** *J-V* curves measured under 1 sun illumination for **a)** DR3-, **c)** PBDB-T-2F-, **e)** PTB7-Th-, and **h)** PBDB-T-SF-based BHJ devices as indicated in the legend. **b, d, f)** and **i)** EQE spectra of the respective devices (see legend for BHJ system). **g)** and **j)** Layout of the device structure of the studied solar cells (inverted was used for PBDB-T-SF- based devices, normal for all other donors).



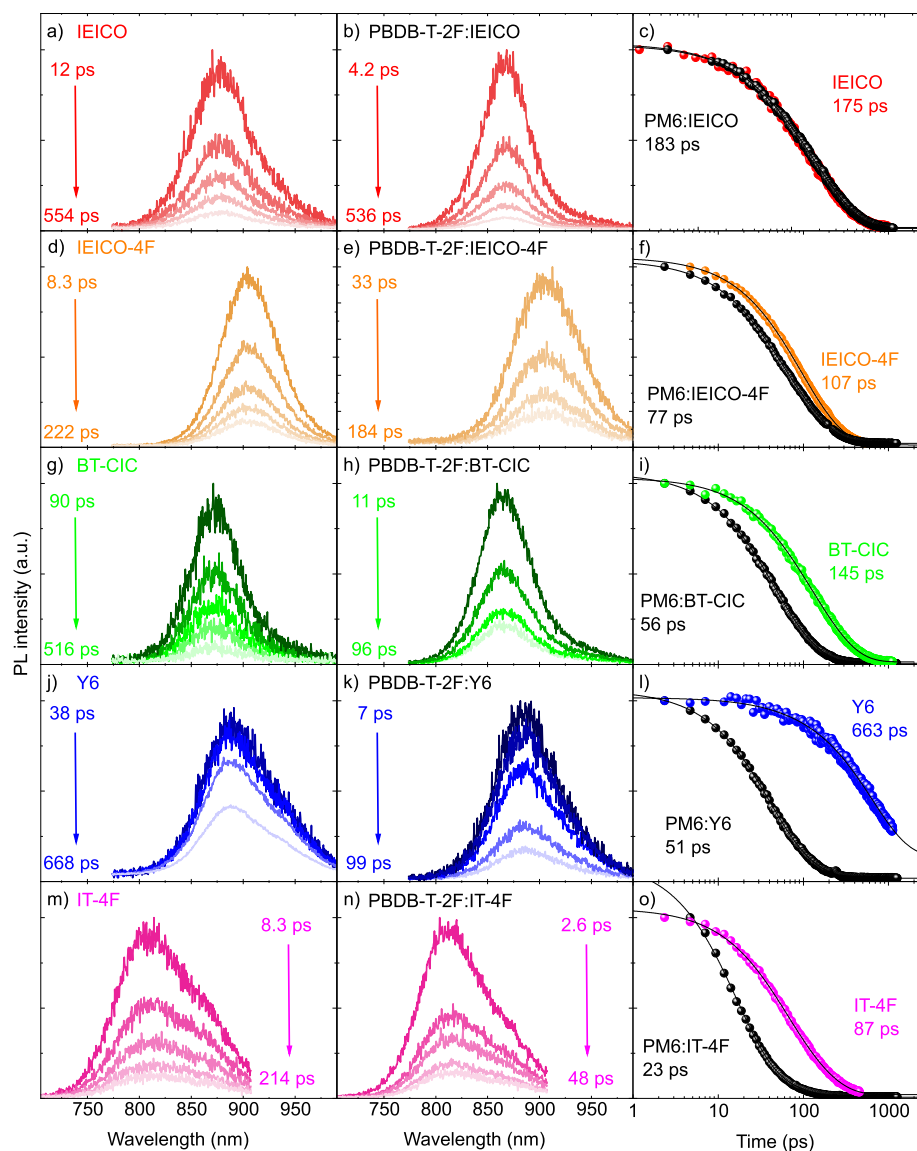
**Extended Data Fig. 5 | Internal quantum efficiency of DR3-, PBDB-T-2F-, PTB7-Th- and PBDB-T-SF-based devices.** Internal quantum efficiency (IQE) spectra of DR3- (a), PBDB-T-2F- (b) PTB7-Th- (c), and PBDB-T-SF-based devices. The IQE of each solar cell was calculated using:  $\text{IQE}(\%) = 100 \cdot \text{EQE}(\%) / (100\% - \text{Reflectance}(\%) - \text{Parasitic Absorption}(\%))$ . The reflectance spectra were collected with an integrating sphere using the same EQE measurement system, while the parasitic absorption was calculated using transfer matrix modelling.



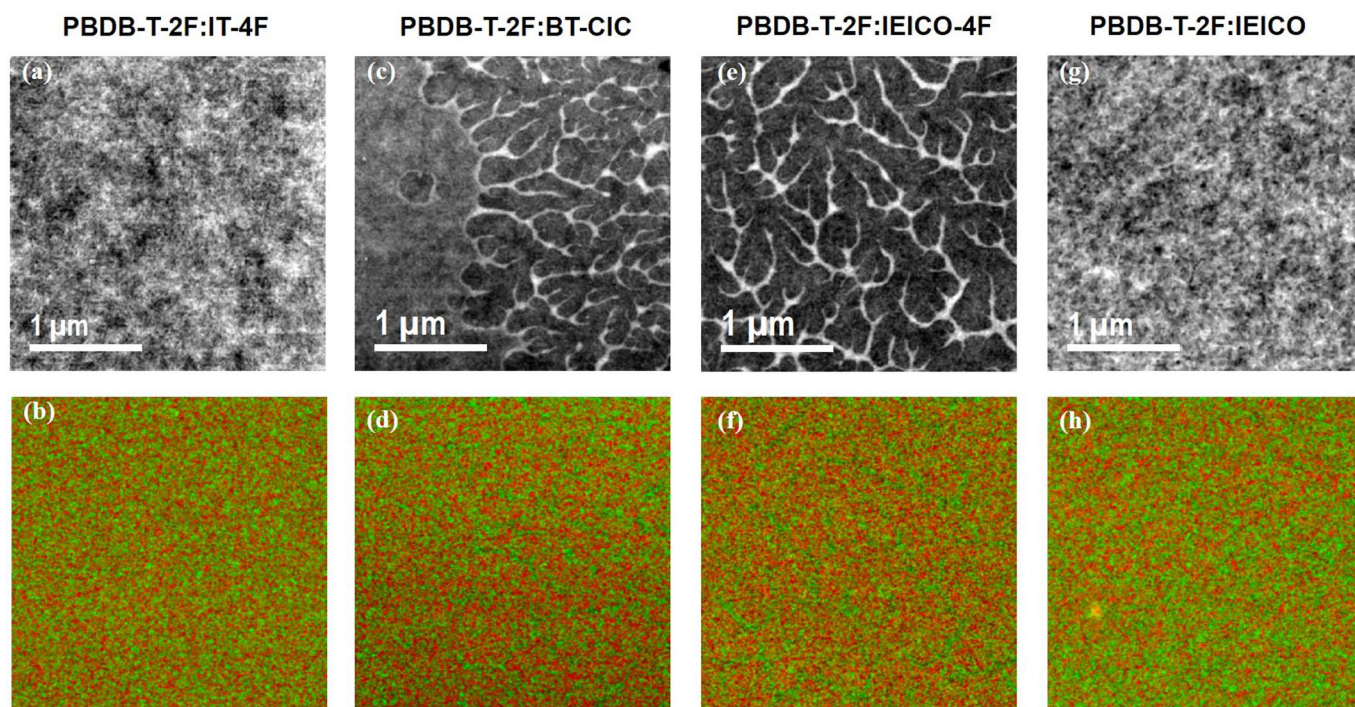
**Extended Data Fig. 6 | Fill factor vs IE offset.** Qualitatively, the solar cells' fill factors (FF) increase with the IE offset in all donor-NFA systems. Quantitatively, the increase depends on the specific donor used.



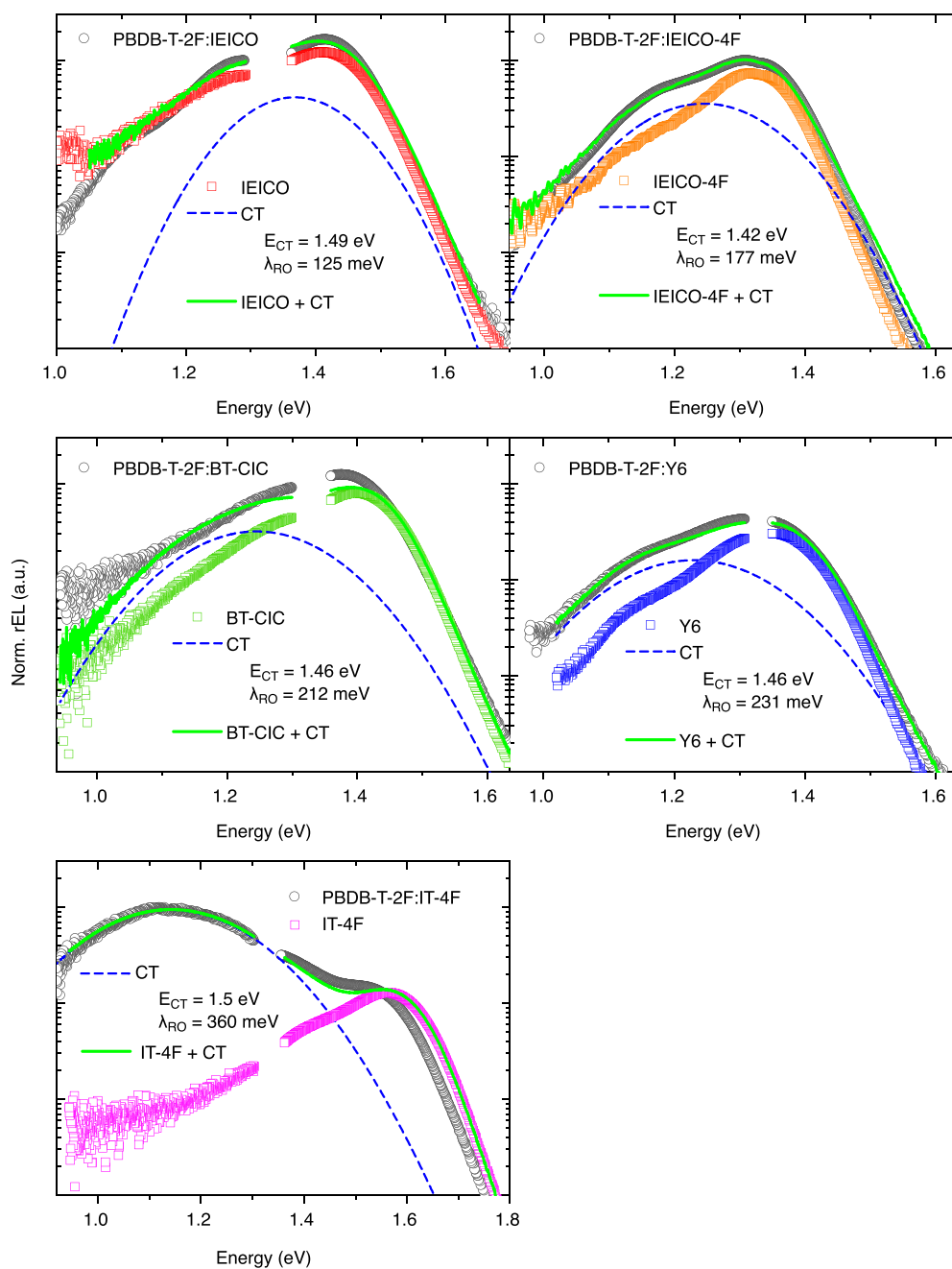
**Extended Data Fig. 7 | Fluence-dependent nanosecond to microsecond TA kinetics of DR3 blends.** Fluence-dependent nanosecond to microsecond TA kinetics of DR3 blends (photo-induced absorption region) as indicated in the legend after excitation at 532 nm. The percentage of free charge generation as obtained from the two-pool recombination model fit to the experimental data is shown in each panel. Details of this calculation can be found in the SI (two-pool charge recombination model).



**Extended Data Fig. 8 | Time-resolved photoluminescence spectra and kinetics of PBDB-T-2F blends and respective neat acceptors.** Time-resolved photoluminescence **a-b, d-e, g-h, j-k, m-n)** spectra and **c, f, i, l o)** kinetics of IEICO and PBDB-T-2F:IEICO, IEICO-4F and PBDB-T-2F:IEICO-4F, BT-CIC and PBDB-T-2F:BT-CIC, Y6 and PBDB-T-2F:Y6, IT-4F and PBDB-T-2F:IT-4F, respectively, under inert nitrogen atmosphere,  $\lambda_{exc} = 690$  nm.



**Extended Data Fig. 9 | Thin-film morphology analyses of optimized IT-4F, BT-CIC, IEICO-4F and IEICO blends with PBDB-T-2F.** Thin-film morphology analyses of optimized BHJ active layers. (a, c, e, g) dark-field STEM image and (b, d, f, h) EELS map of (a-b) IT-4F, (c-d) BT-CIC, (e-f) IEICO-4F and (g-h) IEICO blends with PBDB-T-2F. The EELS maps depict the component-separation as donor-rich (red) and NFA-rich domains (green). Note that 60 - 70 nm thick films were used for these analyses to improve spectral resolution and reduce domain overlap when projected through the film thickness.



**Extended Data Fig. 10 | Electroluminescence spectra of PBDB-T-2F:NFA-based devices.** Reduced electroluminescence spectra of PBDB-T-2F:NFA-based devices (black symbols), their decomposition into neat NFA reduced electroluminescence (colored symbols), and a Gaussian-shape CT state emission (blue dashed lines), and the sum of the two contributions (solid green line). The gap between 1.3 and 1.36 eV corresponds to the spectral region, where both the infrared and visible detector used to measure the EL spectra are less sensitive (about 80% of the maximum sensitivity).

## Solar Cells Reporting Summary

Nature Research wishes to improve the reproducibility of the work that we publish. This form is intended for publication with all accepted papers reporting the characterization of photovoltaic devices and provides structure for consistency and transparency in reporting. Some list items might not apply to an individual manuscript, but all fields must be completed for clarity.

For further information on Nature Research policies, including our [data availability policy](#), see [Authors & Referees](#).

## ▶ Experimental design

## Please check: are the following details reported in the manuscript?

## 1. Dimensions

- Area of the tested solar cells  Yes Described in Methods, section "Thin-film and device preparation".  
 No
- Method used to determine the device area  Yes Described in Methods, section "Thin-film and device preparation".  
 No

## 2. Current-voltage characterization

- Current density-voltage (J-V) plots in both forward and backward direction  Yes Described in Methods, section "Device characterization".  
 No
- Voltage scan conditions  Yes Described in Methods, section "Device characterization".  
*For instance: scan direction, speed, dwell times*  
 No
- Test environment  Yes Described in Methods, section "Device characterization".  
*For instance: characterization temperature, in air or in glove box*  
 No
- Protocol for preconditioning of the device before its characterization  Yes No preconditioning of the devices was done prior to their characterization.  
 No
- Stability of the J-V characteristic  Yes Not verified, as long-term stability is not a critical issue for the claims and conclusions of this study.  
*Verified with time evolution of the maximum power point or with the photocurrent at maximum power point; see ref. 7 for details.*  
 No

## 3. Hysteresis or any other unusual behaviour

- Description of the unusual behaviour observed during the characterization  Yes No unusual behaviour observed.  
 No
- Related experimental data  Yes No unusual behaviour observed.  
 No

## 4. Efficiency

- External quantum efficiency (EQE) or incident photons to current efficiency (IPCE)  Yes Provided in Extended Data Fig. 4.  
 No
- A comparison between the integrated response under the standard reference spectrum and the response measure under the simulator  Yes Not explicitly provided, however, the intensity of the solar simulator was calibrated with a silicon reference cell and its spectral mismatch has been accounted for.  
 No
- For tandem solar cells, the bias illumination and bias voltage used for each subcell  Yes Tandem solar cells have not been reported in this study.  
 No

## 5. Calibration

- Light source and reference cell or sensor used for the characterization  Yes Described in Methods, section "Device characterization".  
 No
- Confirmation that the reference cell was calibrated and certified  Yes Described in Methods, section "Device characterization".  
 No

- Calculation of spectral mismatch between the reference cell and the devices under test  Yes Described in Methods, section "Device characterization".  
 No
6. Mask/aperture
- Size of the mask/aperture used during testing  Yes Device active area specified in Methods, section "Thin-film and device preparation".  
 No
- Variation of the measured short-circuit current density with the mask/aperture area  Yes Not relevant to this study, but the device area has been kept constant for all cells.  
 No
7. Performance certification
- Identity of the independent certification laboratory that confirmed the photovoltaic performance  Yes not applicable  
 No
- A copy of any certificate(s)  
*Provide in Supplementary Information*  Yes not applicable  
 No
8. Statistics
- Number of solar cells tested  Yes 10 cells per system tested. Details provided in caption of Supplementary Table 2.  
 No
- Statistical analysis of the device performance  Yes Values provided in Supplementary Tables 2, 3, and 4 were averaged over ten devices.  
 No
9. Long-term stability analysis
- Type of analysis, bias conditions and environmental conditions  Yes Not performed as not critical to the claims and conclusions of this study.  
 No  
*For instance: illumination type, temperature, atmosphere humidity, encapsulation method, preconditioning temperature*